Correlations between VIMS and RADAR data over the surface of Titan: Implications for Titan's surface properties

F. Tosi [a,*], R. Orosei [a], R. Seu [b], A. Coradini [a], J.I. Lunine [a,c], G. Filacchione [d], A.I. Gavrishin [e], F. Capaccioni [d], P. Cerroni [d], A. Adriani [a], M.L. Moriconi [f], A. Negrão [g], E. Flamini [h], R.H. Brown [i], L.C. Wye [j], M. Janssen [k], R.D. West [k], J.W. Barnes [l], S.D. Wall [k], R.N. Clark [m], D.P. Cruikshank [n], T.B. McCord [o], P.D. Nicholson [p], J.M. Soderblom [i], The Cassini VIMS and RADAR Teams

[a] INAF-IFSI Istituto di Fisica dello Spazio Interplanetario, Via del Fosso del Cavaliere, 100, I-00133 Roma, Italy
[b] Università degli Studi di Roma "La Sapienza", Facoltà di Ingegneria, Dipartimento INFOCOM, Via Eudossiana 18, I-00184 Roma, Italy
[c] Università degli Studi di Roma "Tor Vergata", Dipartimento di Fisica, Via della Ricerca Scientifica 1, I-00133 Roma, Italy
[d] INAF-IASF Istituto di Astrofisica Spaziale e Fisica Cosmica, Via del Fosso del Cavaliere 100, I-00133 Roma, Italy
[e] South-Russian State Technical University, Prosveschenia 132, Novocherkassk 346428, Russia
[f] CNR-ISAC Istituto di Scienze dell'Atmosfera e del Clima, Via del Fosso del Cavaliere 100, I-00133 Roma, Italy
[g] Escola Superior de Tecnologia e Gestão do Instituto Politécnico de Leiria (ESTG-IPL), Campus 2 Morro do Lena – Alto do Vieiro, 2411-901 Leiria, Portugal
[h] Agenzia Spaziale Italiana, Viale Liegi 26, I-00198 Roma, Italy
[i] Lunar and Planetary Lab and Steward Observatory, University of Arizona, 1629 E. University Blvd., Tucson, AZ 85721-0092, USA
[j] Stanford University, Department of Electrical Engineering, 450 Serra Mall, Stanford, CA 94305, USA
[k] Jet Propulsion Laboratory, 4800 Oak Grove Drive, Pasadena, CA 91109, USA
[l] University of Idaho, Department of Physics, Moscow, ID 83844-0903, USA
[m] US Geological Survey, P.O. Box 25046, MS 150, Denver, CO 80225, USA
[n] NASA Ames Research Center, Moffett Field, CA 94035-1000, USA
[o] The Bear Fight Center, 22 Fiddler's Road, P.O. Box 667, Winthrop, WA 98862, USA
[p] Cornell University, Astronomy Department, 610 Space Sciences Building, Cornell University, Ithaca, NY 14853, USA

ARTICLE INFO

ABSTRACT

We apply a multivariate statistical method to Titan data acquired by different instruments onboard the Cassini spacecraft. We have searched through Cassini/VIMS hyperspectral cubes, selecting those data with convenient viewing geometry and that overlap with Cassini/RADAR scatterometry footprints with a comparable spatial resolution. We look for correlations between the infrared and microwave ranges the two instruments cover. Where found, the normalized backscatter cross-section obtained from the scatterometer measurement, corrected for incidence angle, and the calibrated antenna temperature measured along with the scatterometry echoes, are combined with the infrared reflectances, with estimated errors, to produce an aggregate data set, that we process using a multivariate classification method to identify homogeneous taxonomic units in the multivariate space of the samples.

In medium resolution data (from 20 to 100 km/pixel), sampling relatively large portions of the satellite's surface, we find regional geophysical units matching both the major dark and bright features seen in the optical mosaic. Given the VIMS cubes and RADAR scatterometer passes considered in this work, the largest homogeneous type is associated with the dark equatorial basins, showing similar characteristics as each other on the basis of all the considered parameters.

On the other hand, the major bright features seen in these data generally do not show the same characteristics as each other. Xanadu, the largest continental feature, is as bright as the other equatorial bright features, while showing the highest backscattering coefficient of the entire satellite. Tsegihi is very bright at 5 μm but it shows a low backscattering coefficient, so it could have a low roughness on a regional scale and/or a different composition. Another well-defined region, located southwest of Xanadu beyond the Tui Regio, seems to be detached from the surrounding terrains, being bright at 2.69, 2.78 and 5 μm but having a low radar brightness. In this way, other units can be found that show correlations or anti-correlations between the scatterometric response and the spectrophotometric behavior, not evident from the optical remote sensing data.

© 2010 Elsevier Inc. All rights reserved.

* Corresponding author. Fax: +39 06 49934702.
  E-mail address: federico.tosi@ifsi-roma.inaf.it (F. Tosi).

1. Introduction

Titan is the only satellite in the Solar System to have a dense atmosphere, which is composed primarily of nitrogen, with few percent of methane and lesser amounts of other species. This atmosphere is nearly opaque at visible wavelengths, due to absorption by aerosols and gas and scattering by aerosols. However the atmosphere is optically thin to microwave frequencies.

In exploring the surface of Titan, a powerful combination of data from the Cassini Orbiter instruments comes from joint coverage by the multi-mode RADAR investigation and the Visible and Infrared Mapping Spectrometer (VIMS). The Cassini Titan RADAR Mapper, or RADAR, operates at Ku-band (13.78 GHz frequency or 2.18 cm wavelength) and collects linearly polarized low-resolution (several to tens of kilometers) scatterometer, altimeter, and radiometer data as well as high-resolution (down to ~300 m) synthetic aperture radar (SAR) images covering large strips of Titan's surface (Elachi et al., 2004; West et al., 2009; Table 1 gives some details about RADAR). The Visual and Infrared Mapping Spectrometer (VIMS) collects spectral cubes that are more limited in spatial coverage, the best usually a few km in resolution (very rarely a few hundred meters), but covers a large spectral range from 0.35 to 5.1 μm sampled in 352 spectral channels (Brown et al., 2004; Miller et al., 1996; see Table 2 for some details about VIMS). Finally, the Imaging Science Subsystem (ISS) (Porco et al., 2005) provides images of the surface in the 0.93 μm filter at resolutions ranging from several kilometers to ~1 km, once the strong scattering by aerosols has been corrected by image enhancement techniques (Perry et al., 2005).

IR spectroscopy and microwave radiometry and scatterometry are sensitive, to a different extent and at different scales, to the physical structure of the surface. IR spectroscopy measurements are used to determine surface composition, but they are also affected, down to depths of micrometers, by the physical properties of the surface material like roughness, photometric geometry (Hapke, 1993) and porosity (Hapke, 2008). Microwave radiometry and scatterometry measurements are very sensitive to the roughness and porosity of the upper few to tens of centimeters of the observed surface and to the dielectric permittivity of the surface material (e.g. Ulaby et al., 1981, 1982).

Since VIMS is only sensitive to the first few tens of microns of the surface, a coating of few millimeters is enough to mask the spectral signature of the underlying materials. A bigger problem for surface composition is the optically thick absorbing and scattering atmosphere. On Titan, VIMS provides information about the morphology of the surface thanks to seven infrared windows, where the absorption by atmospheric methane is weaker. In particular, high contrast images are acquired at 2 μm, where the scattering by aerosols is much reduced compared to the shorter wavelengths (Sotin et al., 2005; Rodriguez et al., 2006).

Retrieving surface physical parameters from measurements is a problem that has already been treated for Cassini RADAR scatterometry (Wye et al., 2007) and radiometry (Janssen et al., 2009a). Both sets of measurements have also been combined to obtain a more robust estimate of Titan's surface properties (Zebker et al., 2008). Such parameters are keys in studying the geologic processes shaping the surface of the satellite at scales below the resolution of available SAR imagery (e.g. Janssen et al., 2009b; Le Gall et al., 2009).

The integration of IR spectroscopy with such measurements can provide new insights on the origin and evolution of materials forming the surface. The study of the correlation between different regions of Titan observed with different sensors and with different resolutions can provide unique information on surface properties and processes not available from the individual data sets. This work is new in several respects. We use calibrated measurements instead of physical parameters derived from data, as such derivation is usually mediated by models. We choose data from RADAR – scatterometry and radiometry – that are of comparable spatial resolution to the VIMS data sets used here. Finally, we utilize a spectral classification method that, although previously employed for data from the Moon, Mars, and some saturnian icy satellites, has not hitherto been used on Titan data sets. The goal is to derive a general but rigorous classification of the surface of Titan based on the clustering of measurement values in a multidimensional parameter space, and to validate the results by comparing them to what is known from previous analyses of the same data and from other data sets.

1.1. Previous results

Cross comparisons between ISS, VIMS and RADAR images of Titan have been done previously. Global VIMS and RADAR data comparisons have been made in order to check for systematic correlations related to surface properties (Soderblom et al., 2007; Barnes et al., 2007a). Soderblom et al. (2007) found that RADAR-dark longitudinal dune fields, seen in equatorial to mid-latitudes SAR images, are highly correlated with VIMS "dark brown" units in RGB color composites made from the 2.0 μm, 1.6 μm and 1.3 μm images. This dark-brown unit, relatively dark in all methane windows (Barnes et al., 2007a), shows less evidence of water ice, and it is clearly one of the spectral end members of the surface. On the other hand, water ice as one of the abundant compositional end members of Titan's surface materials is a reasonable candidate; this unit is in fact represented by the "dark blue" material, which is dark at 1.6, 2.0, and 5.0 μm relative to other terrains on Titan, but moderately reflective at 1.3, 1.08, and 0.94 μm (Barnes et al., 2007a). This spectral trend is consistent with water ice, present as

Table 1
RADAR scatterometer operational characteristics. From Wye et al. (2007).

Frequency (wavelength)	13.78 GHz (2.18 cm)
Power transmitted	48.084 W
Peak gain	50.7 dB
Beamwidth (one-way)	0.373° circular
High-gain antenna area	4.43 m^2
Polarization	Same-sense linear (SL)
Receiver bandwidth	117 kHz
Sampling frequency	250 kHz
Signal waveform	Burst of 8 chirp pulses
Burst repetition period	0.47–1.46 s
Pulse length	0.5–0.58 ms
Pulse bandwidth	92.3–105.5 kHz
Pulse repetition frequency	1.202 kHz
Pulse duty cycle	0.6 or 0.7

Table 2
VIMS specifications summary.

	VIMS-V	VIMS-IR
Spectral coverage (μm)	0.35–1.05	0.85–5.1
Spectral channels (bands)	96	256
Total FOV (°)	1.83 × 1.83	1.83 × 1.83
Total FOV (mrad)	32 × 32	32 × 32
Nominal IFOV (mrad)	0.50 × 0.50	0.50 × 0.50
Hi-res IFOV (mrad)	0.167 × 0.167	0.25 × 0.50
Average spectral sampling (nm)	7.3	16.6
Detector type	Si CCD (2D)	InSb photodiodes (1D)
Average SNR	380	100

surface exposures, either in patches or intimately mixed with other components. As an example, the Huygens probe landed in a dark blue unit compatible with the presence of water ice (Tomasko et al., 2005; Rodriguez et al., 2006; Soderblom et al., 2007), although the Gas Chromatograph Mass Spectrometer (GCMS) onboard Huygens found the landing site to contain volatile hydrocarbons and a few additional components (Niemann et al., 2005).

However, the correlation between the two VIMS and RADAR data sets is not systematic in the most general case. The absence of correlation between RADAR and VIMS bright units, found in particular at the Huygens landing site (observed by both instruments, with a ~15 km/pixel resolution by VIMS: see Rodriguez et al., 2006), was interpreted as the result of an optically thick bright mantling which might be transparent to the radar. Though the particular composition of this "bright neutral" end member material is difficult to specify, as a plethora of solid organics form in the upper atmosphere from energetic chemistry, Soderblom et al. (2007) hypothesized that a reasonable candidate is a mantling deposit of aerosol dust that might include acetylene and other simple hydrocarbon solids, whereas the dark brown, water ice-poor end member of the dunes may have a higher concentration of the more complex hydrocarbons and/or nitriles.

Barnes et al. (2007b) investigated the relationships between VIMS and RADAR imagery on an equatorial region east of Xanadu using data from Cassini's ninth and eighth Titan flyby, respectively. Sinuous fluvial features ("channels") have been observed in the two data sets, showing that VIMS was able to detect channel materials despite sub-pixel channel measured widths (~1 km). Especially near their mouths, the channels considered share spectral characteristics with Titan's dark blue terrain, consistent with an enhancement of water ice. On this point, Barnes et al. (2007b) hypothesize that, of the organic haze that settles onto the surface, the soluble portion could be moved by methane rainfall and preferentially washed into channels and then out into the dark blue spectral unit, leaving behind the insoluble portion. Barnes et al. (2007b) also identified that areas east of Xanadu, shown to be mountainous by RADAR, appear darker and bluer than surrounding terrain when observed by VIMS. They interpret this spectral variation as the result of a thin surficial coating that may be present on the surrounding equatorial bright terrain but either diminished in extent or depth or absent entirely within the elevated areas.

Only a few impact craters (or circular features possibly related to impact processes) have been unambiguously detected on Titan by Cassini–Huygens during its nominal mission, which indicates that the surface of Titan is geologically young (Porco et al., 2005; Lorenz et al., 2007; Wood et al., 2009). Lopes et al. (2007) made a distinction between impact craters and calderas of volcanic origin: an impact origin is suggested by the size and the circularity of the features, while cryovolcanic calderas are generally noncircular, with unidirectional flows emanating from the center.

Le Mouélic et al. (2008) have shown that interesting correlations can be observed between the spectrally distinct areas identified in the infrared data and the SAR images of impact craters. As an example, several units appear in VIMS false color composites of band ratios in the Sinlap area, suggesting compositional heterogeneities. The dark (in infrared) crater floor corresponds to the unit delimited by the crater rim in the SAR image, with possibly a central peak identified in both. Both VIMS ratio images and dielectric constant measurements suggest the presence of a dark bluish parabolic area enriched in water ice around the main ejecta blanket. Since the Ku-band SAR may see subsurface structures at the meter scale, the difference between infrared and SAR observations can be explained by the presence of a thin layer transparent to the radar.

In general, the correlation between near-infrared and SAR features is not systematic, which can be explained through the different response of the two wavelength regimes to surface properties

and the depths to which they sample. The two data sets provide very complementary information about surface properties, at nearly all scales.

1.2. Method

We do not use SAR images in this work; instead we apply a multivariate statistical analysis to a set of data made up of infrared spectra acquired by VIMS and scatterometry data and simultaneous radiometry data measured by RADAR.

In order to compensate for the possibility that parts of Titan's surface were unexpectedly radar-dark, and to ensure credible measurements of the surface backscatter variations, a dedicated scatterometer mode was incorporated into the overall RADAR design (Elachi et al., 2004). The scatterometer mode's coarse-resolution, real-aperture operation supplements SAR coverage because the large resolution element provides a stronger reflected signal, increasing the maximum observational distance to about 25,000 km (Wye et al., 2007) and thus permitting imaging of large areas of the satellite. In addition to larger surface coverage, scatterometry also allows backscatter measurements over a wider range of incidence angles, from near-nadir up to 80° or more; such an angular coverage is crucial for parameterizing surface properties (Wye et al., 2007). The Cassini RADAR instrument also includes a passive radiometer that operates in all modes of the instrument (Elachi et al., 2004; West et al., 2009), measuring the 13.8 GHz emissivity of Titan and other targets of opportunity. Both of these modes provide information at spatial resolution more comparable to that of the VIMS data we have examined than does the SAR mode.

We have considered five Titan flybys that occurred in the first 2 years of nominal mission, referred to as T3, T4, T8, T13 and T16 in the following. T3 scatterometry embraces a broad range of latitudes near the prime meridian; T4 covers a relatively small portion of terrain north of the Fensal dark equatorial basin; T8 scatterometry overlaps with most of the Shangri-La dark equatorial basin, a wide portion of Xanadu and a small portion of the two Adiri and Dilmun bright features; T13 crosses the southern portion of the Shangri-La equatorial basin and surrounding bright features; finally T16 covers the Dilmun bright feature, the northern portion of the Shangri-La basin and the northern border of Xanadu.

After selecting VIMS data with a spatial resolution comparable to that of the scatterometry footprints and proper illumination conditions, we have compared these data with the five RADAR passes cited above in order to look for overlaps, which in fact have been found for 405 VIMS cubes, from mission sequences: S05 (Ta), S06 (Tb), S08 (T3), S15 (T8), S17 (T9–T10), and S29 (T28).

A first analysis on a small subset of these data has been performed with the G-mode clustering method (briefly described in Section 5), which has been successfully used in the past for the classification of such diverse data sets as lunar rock samples, asteroids, Mars and other icy saturnian satellites. A key advantage is that the G-mode is an unsupervised method, so it can be used without any a priori knowledge of the taxonomic structure of the observations, which is in fact provided by the classification.

2. RADAR data selection

Scatterometry and radiometry data from RADAR passes T3, T4, T8, T13, and T16 were selected for this work. Such data, stored in the RADAR *Burst Ordered Data Products* (BODP) archives, contain calibrated measurements from flyby Ta to flyby T19, i.e. from 26 October 2004 to 9 October 2006 at the time of this analysis. Ta, namely the first Titan flyby, was discarded because scatterometry scans suffered from clipping towards the center of the scan lines

(where the incidence angle is low) due to faults in the auto-gain algorithm. Other flybys up to T19 have been also discarded, because they do not contain scatterometry data, or they contain only distant radiometry data that are useless for our purpose because they have a rather low spatial resolution, generally unsuited to a correlation with most VIMS data. Therefore, before T19 or before 9 October 2006, the only data satisfying our requirements are those of the flybys: T3, T4, T8, T13 and T16. Flybys occurring after 9 October 2006 were not taken into account for two reasons: (1) five RADAR passes provide a sufficient coverage and therefore a significant statistical sample to test the classification method and evaluate its results and (2) five RADAR passes provide a sufficient number of overlaps with the VIMS data available at the time this work was undertaken (see Section 3).

In the above-mentioned flybys, the scatterometer scanned the disk of Titan, sometimes in the inbound phase, sometimes in the outbound phase, and in one case in both phases of the flyby. Some details concerning these observations are summarized in Table 3.
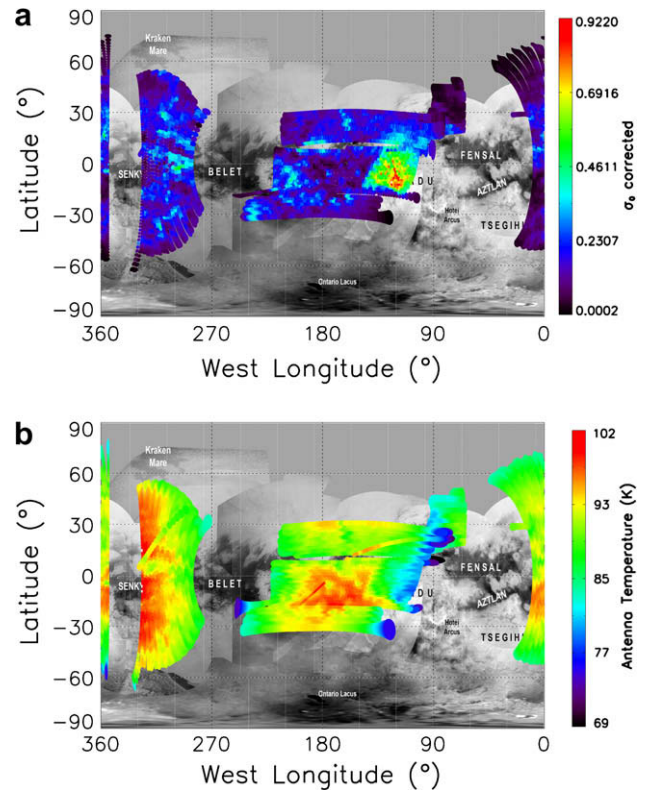
Fig. 1 shows the simple cylindrical projections of the scatterometry footprints' on the mosaic map of Titan produced by the ISS team on the basis of the best images acquired in the infrared filter centered at 0.938 μm (Turtle et al., 2009) in the period April 2004 through August 2008. On this point, it should be noted that, strictly speaking, the geometries computed for the scatterometric and simultaneous radiometric data are actually different, because the geometries associated with the active and passive modes refer to two different times (the median point between the centers of the two transmission and receiving windows and the center of the receiving window, respectively). However, in practice these two moments are very close to each other, so we assume that the scatterometric and concomitant radiometric footprints are roughly coincident, and the incidence and emission angles are the same (differences can change from flyby to flyby depending on the specific geometry, but in any event they stand rather low – i.e., less than 2° – for the five flybys considered here).

After the selection of the RADAR data suitable for combining with the VIMS data set, it is necessary to retrieve the geometric information for their projection. The geometric data for each scatterometric and radiometric footprint are already computed and stored in the SBDR (*Short Burst Data Records*) files, since the process by with they are prepared is part of the intermediate segment of the calibration pipeline involving the BODP data. Geometries are computed through the standard SPICE system (Acton, 1996), assuming Titan as a 2575 km-radius sphere, using the most reliable ephemerides available for the spacecraft (reconstructed *a posteriori* from telemetry data), and following the IAU convention about the longitudes (increasing westward in the range 0–360°).

Fig. 1. Simple cylindrical projection of the RADAR scatterometric (a) and radiometric footprints (b) used in this work (from Titan flybys: T3, T4, T8, T13 and T16), superimposed to an optical mosaic of Titan derived from the best ISS images (Turtle et al., 2009). The color code is related to the σ_0 backscattering coefficient (above) and the calibrated antenna temperature (below), respectively.

2.1. RADAR data calibration

In Cassini/RADAR data, the *normalized radar cross-section* (NRCS), indicated with σ_0, is a dimensionless quantity expressed in the physical (linear) scale, not in the dB (logarithmic) scale. σ_0 is determined by the dielectric and geometric properties of the scatterers located in the illuminated area, is related to the received power by means of the radar equation and is acquired in all of the active modes used by the Cassini Titan RADAR Mapper (West et al., 2009). Being the backscattering coefficient calibrated through the radar equation, it is not dependent on the target range and thus on the size of the radar resolution cell, antenna gain, position in

Table 3
Characteristics of the scatterometric RADAR passes used in this work.

	T3	T4	T8	T13	T16
Flyby date	15/02/2005	31/03/2005	28/10/2005	30/04/2006	22/07/2006
Flyby phase	Outbound	Inbound	Inbound and outbound	Outbound	Inbound
Relative velocity (km s^{-1})	6.1	5.9	5.9	6.0	6.0
Max res. major axis (km)	200.158	310.909	307.438	366.019	195.204
Min res. major axis (km)	44.747	87.445	44.139	63.203	73.930
Mean res. major axis (km)	88.103	138.138	99.945	135.148	132.464
±σ res. major axis (km)	28.950	32.253	36.305	48.255	28.692
Burst ID start	45013503	48018174	65014558	82023290	87022589
Burst ID stop	45015414	48021241	65028990	82025928	87026480
Valid bursts	1759	2931	3746	2431	3538
Duration (s)	1873	2220	5743	2381	2793
θ_i min (°)	2.006	32.802	0.684	22.327	0.062
θ_i min (°)	76.645	76.933	80.428	77.387	77.623
σ_0 min	0.00344	0.00024	0.01304	0.00508	0.00158
σ_0 max	0.52728	0.35843	0.92200	0.42246	0.47773
T_a max (K)	74.855	74.993	68.640	73.711	71.131
T_a min (K)	97.933	92.084	101.988	97.104	96.190

antenna pattern, transmitted power and wavelength; however it is function of the incidence angle.

It should be noted that no backscattering coefficient model (e.g., Gaussian, Hagfors, exponential laws) is applied to the data: the NRCS is "the backscatter coefficient", not a model dependent quantity. However, the public Planetary Data System (Website of the NASA"s Planetary Data System database) RADAR products include both an uncorrected σ_0 value and an "incidence angle corrected" value. When this work was carried out, the formula used for this correction was such that the correction factor is 1.0 at an incidence angle of 45° (Stiles, personal communication, 2007):

$$\sigma_{0,corr} = \sigma_0 \cdot \sqrt{2} \sin \theta_i \qquad (1)$$

where σ_0 is the calibrated, uncorrected backscattering coefficient and θ_i is the incidence angle. In this way, the corrected $\sigma_{0,corr}$ value is assumed to be equal to the uncorrected value for an incidence angle of 45°; for smaller angles it is decreased whereas for larger angles it is proportionately increased. Such a correction, which is adopted in the data used here, is a reasonable normalization in that it emphasizes the presence of microwave-reflecting structures in a broad range of situations involving the remote sensing of geologic targets.

Recently, Wye et al. (2008) derived a better correction, given by a superposition of large-scale surface scattering (quasispecular scattering) together with a combination of small-scale surface scattering and subsurface volume scattering (diffuse scattering). This correction will be applied in the reprocessing pipeline of RADAR data.

3. VIMS data selection

VIMS data of Titan from mission sequence S01 to mission sequence S29 (June 2004 through April 2007) have been considered in this work. This represents a total of 10,113 cubes. Further sequences were not considered because they were still not available when this work was undertaken. The data set we do use is sufficient for statistical purposes. Among available data, we choose only those with the following characteristics: a resolution with an upper limit comparable to the resolutions of the RADAR scatterometric footprints, a low phase angle (intended to select only cubes showing most of the dayside, and to limit the dependence on the specific observational geometry), and a good signal-to-noise ratio (SNR). To do this, we select cubes that show all of the following: (1) a spatial resolution ⩽200 km; (2) a phase angle ⩽40°; (3) an IR exposure time ⩾160 ms/pixel.

It turns out that the VIMS cubes satisfying the above criteria are 222 with nominal Instrumental Field of View (IFOV) of 0.50 × 0.50 mrad and 183 with hi-res IFOV (0.25 × 0.50 mrad), for a total of 405 cubes, i.e. about 4% of all the Titan cubes in the phase of the mission considered. Table 4 gives details on these data. On all of these cubes, the *Integrated Software for Imagers and Spectrometers* (ISIS) was ap-

plied in order to retrieve the geometric parameters of each VIMS pixel showing an intercept with the solid surface of the target. It should be noted that, in order to do this, the new RADAR-determined Titan pole location (Stiles et al., 2008) was applied.

3.1. VIMS data calibration

All of the VIMS cubes used in this work are calibrated by means of the RC15 VIMS-IR sensitivity function and the 2005 flat-field cube, namely the latest official products available at the time this work was undertaken. The sensitivity function is used to convert the raw signal of each pixel inside the IR image into radiance (divided by the IR integration time and the flat-field) and then into reflectance I/F, where I is the intensity of reflected light and πF is the plane-parallel flux of sunlight incident on the satellite (Thekaekara, 1973), scaled for its heliocentric distance (for details about the VIMS calibration, see McCord et al. (2004)).

4. Data fusion project

The basic idea of this work is to generate a data set in which the samples are the observations (i.e., pixels) of VIMS, while the variables are the reflectances (I/F) measured in some of the methane windows of Titan; to these variables we combine the normalized backscatter cross-section (i.e., the backscattering coefficient) measured by RADAR and, when appropriate, also the calibrated antenna temperature measured along with the scatterometry echoes. Such a data set is processed by a clustering method able to automatically discriminate groups of pixels similar to each other on the basis of all the considered variables, so that correlations or anti-correlations among the physical processes explored in the different spectral ranges of the two instruments can be identified. However, the calibrated backscattering coefficient is a function of the incidence angle, so a proper correction for this parameter has to be applied as discussed in Section 3.

The radiant power collected by the antenna and input to the radiometer is defined as the antenna temperature. The antenna temperature, also stored in RADAR data, is measured by the instrument without any correction apart from the standard calibration (West et al., 2009), and for a given direction it is modeled by the brightness temperature and the gain of the antenna. From the theory of radar radiometry, it is found that the brightness temperature of a spherical target is a function of the polarization, of the dielectric constant and also of the surface roughness in the general case (Heiles and Drake, 1963; White and Cogdell, 1973). The brightness temperature is related to the physical (thermodynamic) temperature by means of the emissivity, which in turn is a function of the dielectric constant for a given polarization (horizontal or vertical). Since the antenna temperature includes a contribution from the sidelobes that needs to be accounted for, it is always higher (by as much as 10 or more Kelvin) than the brightness

Table 4
Characteristics of the VIMS data set used in this work.

Sequence	Flyby	Nominal IFOV			Hi-res IFOV		
		Number of cubes	Mean phase angle (°)	Mean resolution (km/pixel)	Number of cubes	Mean phase angle (°)	Mean resolution (km/pixel)
S05	Ta	74	13.912	71.688	8	13.119	62.660
S06	Tb	–	–	–	82	16.169	63.658
S08	T3	73	19.874	96.384	–	–	–
S15	T8	5	23.225	69.068	–	–	–
S17	T9–T10	43	27.230	63.354	75	34.603	75.188
S29	T28	27	36.615	93.271	18	36.398	115.986
Total		222			183		

temperature. The latter results from the calibration approach that treats the far sidelobe contributions as an additional signal to be removed through analysis (see Section 2.2 of Janssen et al. (2009a)).

Differences in the backscattering coefficient and in the antenna temperature may be indicative of the dielectric constant of surface material, and the weight of this parameter shall be evaluated from case to case. Recently, a map of dielectric constants for the surface of Titan has been derived by the RADAR radiometer team (Janssen et al., 2009a), which was not yet available when this work was undertaken. In the future, RADAR data will be reprocessed and delivered taking into account this important outcome (West, personal communication, 2008). However, the differences in antenna temperature among different regions on Titan are supposed to be quite reliable also before this kind of reprocessing, especially when looking at reasonable emission angles (Janssen, personal communication, 2008), so in this work we will focus especially on temperature differences among homogeneous types, rather than on absolute values of the temperature.

On the imaging spectroscopy side, the spectrum of Titan as observed by VIMS is dominated by the absorptions of methane in the visual and near-infrared ranges. In both cases, it is possible to identify the "atmospheric windows", where the absorption of solar radiation by the atmosphere is lower and the measured reflectance I/F is accordingly higher: in these wavelengths, the smaller opacity reveals albedo differences due to the reflection of solar radiation by the surface.

In principle, a complete sampling of the I/F in the VIMS spectrum could be performed in all of the methane windows between 0.35 and 5.1 μm. However, here we do not consider the visible range, mainly because visible wavelengths are affected by the Rayleigh scattering in gaseous nitrogen and methane; the mitigation of this effect in the data requires a complete radiative transfer treatment for the atmosphere. Furthermore, also in the near-infrared range we discarded the wavelengths shortward of 2 μm, because they are significantly affected by the Mie scattering induced by the aerosol haze which has a typical particle size of the order of the wavelength. In the Mie scattering regime, the wavelength dependence is essentially imposed by the refractive indices of the particles, but it is generally weaker than the Rayleigh scattering, so that rudimentary corrections to reflectance data can be attempted (e.g., see Rodriguez et al., 2006; McCord et al., 2007; Barnes et al., 2009; Hayne et al., 2009).

From Earth-based, high-spectral resolution observations, as well as from theoretical models developed before the Cassini arrival at Saturn, it has been possible to characterize the behavior of these aerosols. In this way it is seen that, because they mainly scatter at the shorter wavelengths, their transmittance increases towards the longer wavelengths (Negrão, 2007); so, given the spectral range covered by VIMS, the best wavelength region to restrict the effect of the haze scattering and sample the surface of Titan is between 2 μm and 5 μm (the extinction coefficient of aerosols reaches a minimum at about 2 μm, but the computation of the spectral transmittance also takes into account the average particles size, so that the transmittance is greater at 5 μm). In conclusion, in the IR spectrum measured by VIMS, we discarded the windows at 0.9331, 1.0818, 1.2781 and 1.5902 μm, providing a complementary information but characterized by a smaller transmittance due to the higher magnitude of this effect, whereas we considered the windows centered at the wavelengths of 2.0178, 2.6962, 2.7812 and ~4.97 μm, respectively (in the following text, for conciseness we tag these wavelengths with the numbers: 2.02, 2.69, 2.78 and 5 μm). Such a choice complicates a direct comparison with the results described in Soderblom et al. (2007) and less quantitatively in Barnes et al. (2007a), who also used the 1.28 and 1.59 μm windows, especially in the evaluation of differ-

ences between the "dark brown" dune material and the "dark blue" icy unit, but at the same time ensures that our results are not affected by the atmosphere.

The first of these methane windows, at 2.02 μm, has the most surface contrast, being only barely sensitive to residual aerosol haze scattering; moreover VIMS shows a good instrumental SNR at this wavelength. The 2.8 μm methane absorption window, where the radiance amount as well as the instrumental SNR are rather low, is complex: data from the Infrared Space Observatory (ISO) first suggested, and the VIMS spectra confirmed, the existence of two subwindows peaked at 2.69 and 2.78 μm, rather than one "clean" broad window from 2.7 to near 3.1 μm, divided by an absorption of unknown origin (Coustenis et al., 2006; McCord et al., 2006). Since the aerosol scattering is gradually less effective towards the longer wavelengths, in the VIMS spectral range the 5 μm window is a natural candidate in order to sample the surface of the satellite. However, at 5 μm the measured radiance is generally low, though higher than in the double-peaked 2.8 μm window. Moreover VIMS' last spectral channels are characterized by a higher instrumental noise, so, in order to increase the SNR, we actually considered the average of the last 15 channels between 4.8855 μm and 5.1225 μm, except the third last channel at 5.0911 μm, showing a very poor SNR, in a way similar to what was already done in previous works (Barnes et al., 2007a).

Only pixels with favorable observational and illumination conditions are selected: i.e., those having a phase angle <40°, and incidence and emission angles <60°. The reason of the upper limit for the phase angle is to ensure that most of the dayside is seen, and to limit the dependence on the observing conditions, while an upper limit on the solar incidence angle is set in order to ensure that the selected pixels are seen with a fair solar illumination (far enough from the terminator, in order to have a good SNR) and in a limited range of local times. On the other hand, the upper limit on the emission angle lies in the fact that, in Titan images, contrast decreases with increasing emission angle, with a decrease that seems to be approximately linear with emission angle (Fussner et al., 2005). From 0° to 60° emission angle, the optical depth of haze changes by a factor of two, meaning that light leaving the planet from 60° emission angle must pass through twice as much haze as light leaving at 0°. Therefore, we discarded pixels with an emission angle >60° because they are unfavorable from a radiometric point of view. Another constraint on the emission angle is that of warping of the VIMS projected pixels. In fact, because by definition the emission angle is 0° in the sub-observer (nadir) point while it increases towards the limb of the target, and since the projection of VIMS pixels is more and more warped as they fall near the limb of the target (in proportion to the sine of this angle), an emission-angle-based selection allows one to leave out VIMS footprints with a strong geometric distortion and hence low signal.

By plotting the position of the selected VIMS pixels' centroids with a color code related to the reflectance in the two methane windows at 2.02 μm and 5 μm, it is possible to point out the good agreement generally existing between the major bright and dark features seen in the "optical" images mosaic, derived from the images acquired by the ISS camera onboard Cassini, and the reflectances measured by VIMS in the same regions (Fig. 2), and it is possible to verify the peculiar behavior of some features: for example, we find that the Tui Regio south of Xanadu is very bright at 5 μm, consistently with previously published works (Barnes et al., 2005, 2007a).

Once the best VIMS and RADAR data have been selected, they are examined to find overlaps between the two data sets. Preliminary shapes for Titan have been derived (Zebker et al., 2009), but until a final geoid is defined on the basis of comprehensive RADAR data, the satellite's shape is assumed to be a sphere with a radius of 2575 km, so that it is easy to move from planetocentric angular
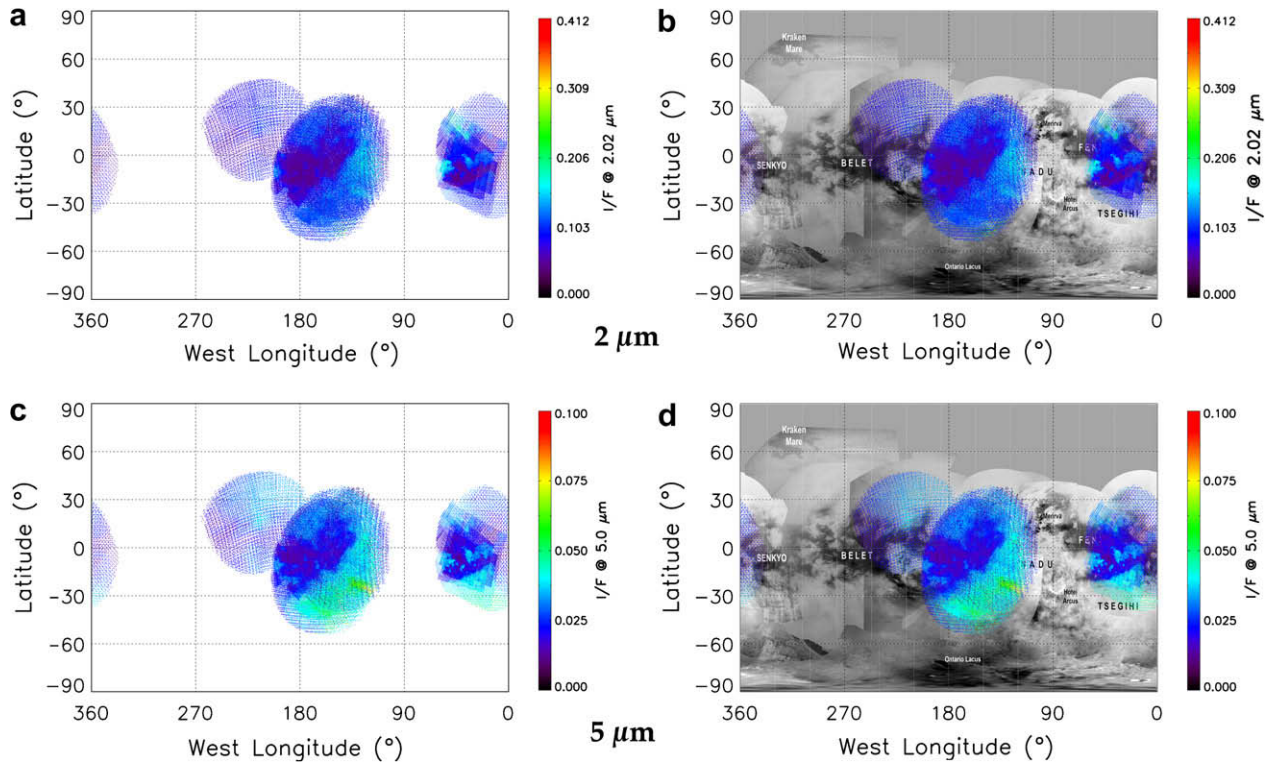
Fig. 2. Distribution of VIMS observations (pixels) considered in this work (from sequences: S05, S06, S08, S15, S17, and S29), selected by constraining the illumination angles (<60°) and the phase angle (<40°). (a) Reflectance measured at 2.02 μm; (b) reflectance at 2.02 μm overlapped with an ISS optical mosaic; (c) reflectance I/F measured at 5 μm (average of 14 spectral channels); (d) reflectance at 5 μm (average of 14 spectral channels) overlapped with an ISS optical mosaic.

coordinates, namely longitude and latitude, to cartesian coordinates expressed by a bidimensional array of fixed resolution. Because in this case on a great circle of Titan 1° = 44.942 km, assuming that the overall surface has to be represented by a grid with a spatial resolution of 1 km, then the array representing the surface of Titan will have dimensions of 16,180 × 8090 elements, given by 360° × 44.942 for the longitude and 180° × 44.942 for the latitude, respectively.

It is worthwhile noticing that such a grid is not a real projection, but rather a representation: moving from the equator to the poles, the parallels' length decreases in proportion to the cosine of the latitude. Having rows with the same number of elements (or parallels with the same length, i.e. 16,180 km long) simply means that, although any line of the grid has the same number of elements, from the equator to the poles a growing number of these elements are blank because the relative distances among the footprints' centroids tend to increase.

The geometries computed for both the VIMS and RADAR data can be referred to this grid. Like in the case of the simple cylindrical projection and of the Mercator and Miller projections, this representation also has the drawback of being warped in the polar regions. On the other hand, in the data set used in this work, the polar regions are never covered by the two instruments, so this representation is adequate. Moreover, it is convenient to choose the origin of this grid in the south pole (latitude −90°) rather than on the equator, because in this way the grid indices defining the latitude in kilometers always have a non-negative value, thus being better handled as arrays by the computational procedures developed for this work.

The use of a matrix format has a benefit in the data analysis. If both the VIMS and RADAR geometries are stored as bidimensional arrays with the same dimensions, simple Boolean operations can be used to find out coordinates common to the two data sets: if such arrays consist of integer numbers with value 0 if the (x, y) element has no data or value 1 if it corresponds to an observed point, in the array resulting from the "AND" operation, the elements having value 1 are only those having value 1 in both of the two operand arrays. Through such operations, it is possible to check for overlaps in the data set.

5. The classification method

Multivariate analysis is very useful in the case of hyperspectral data like those acquired by VIMS, showing a large information content. When the samples are represented by spectral observations, typically a large number of spectra are averaged in order to increase the SNR; in our approach, averages are made only on subsets of samples that are statistically close to each other on the basis of the most meaningful variables. For classifying our aggregate data set, here we used the *G-mode* unsupervised clustering method.

The *G-mode* method was originally developed by Gavrishin and Coradini (see Gavrishin et al., 1980, 1992; Coradini et al., 1976, 1977) to classify lunar samples on the basis of the major oxides composition. The good results obtained for lunar material warranted its application to several different data sets (see, for example, Coradini et al., 1976, 1983; Carusi and Massaro, 1978; Bianchi et al., 1980; Gavrishin et al., 1980; Giovannelli et al., 1981; Barucci et al., 1987; Orosei et al., 2003). In particular, the Imaging Spectrometer for Mars (ISM), flown onboard the Soviet Phobos mission, offered the first chance to apply the *G-mode* method to imaging spectroscopy data (Coradini et al., 1991; Erard et al., 1991; Cerroni and Coradini, 1995). More recently, the *G-mode* was applied also to Cassini/VIMS data relative to Phoebe (Tosi et al., 2005; Coradini et al., 2008) and to other icy saturnian satellites (Tosi et al., 2010).

Details on the method are given in Gavrishin et al. (1992). The G-mode differs from other broadly used unsupervised statistical methods – such as the Principal Components Analysis (PCA) and the Q-mode method – in some key characteristics (see Bianchi et al., 1980). A linear dependence of the variables is not needed; second, instrumental errors can be taken into account; third, meaningless variables are discerned and removed; and finally different levels of classification can be performed.

In summary, given a multivariate population characterized by N samples each depending on M variables, the frequency distribution for each variable – provided that the population is homogeneous – will follow a Gaussian distribution law. Hence it can be assumed that each homogeneous group represents a specific physical process and that the deviation from the average is due only to the intrinsic fluctuation of the process of the physical process under investigation, namely to the statistical errors. Overlapped with the statistical error, the measurement error should be taken into account. The G-mode in fact uses the instrumental error of provided in input by the user when this is greater than the intrinsic standard deviation of the variable itself. Furthermore, independence of variables and samples is not required, although the relationship between variables and samples needs to be known.

Once the barycenter of the first homogeneous type has been identified (which in the G-mode is represented by the three closest samples on the basis of all variables), then a peculiar function is used to collapse each multivariate sample into an equivalent univariate Gaussian distribution, that is compared with another normalized Gaussian distribution obtained with the "q threshold", provided in input by the user. Given that the classification criterion is based on a statistical test, the critical value expressed by q in fact represents the confidence level of the test: the higher the value of q the broader, or more general, is the classification for given errors; conversely, the smaller the q, the more detailed it is. Therefore, by changing this critical value it is possible to get different levels of classification and correspondingly different degrees of class homogeneity (Gavrishin et al., 1992). In particular, by lowering the confidence level of the test, set *a priori* by the user, the algorithm can perform a more refined classification, in order to look for further homogeneous types. In this case, the G-mode includes a test that allows one to interrupt the classification when it becomes too detailed. When the statistical distance among types becomes smaller than the established confidence level, the algorithm can either stop or continue by merging different small types together (such a condition is reported in the output of the program).

Finally, for all variables a statistical weight is computed at the end of the processing, after all the homogeneous types have been found. For each variable this weight is given by the ratio between the ith element ($i = 1, \ldots, M$) of the symmetric distance matrix – representing the statistical (Euclidean) distances of each homogeneous type with respect to the others on the basis of all the meaningful variables – and the summation of all the elements of the matrix from 1 to M.

In principle, in the G-mode we can apply the instrumental noise of each spectral channel of VIMS as an instrumental error to be applied to each spectrophotometric variable. Nevertheless, it should be noted that for these variables we prefer to apply an absolute instrumental error (0.001), because VIMS-IR is affected by a larger instrumental noise towards the longer wavelengths: since the 5 μm window has to be as relevant as the 2 μm window for the classification, an absolute error ensures that the clustering analysis is not misled. Furthermore, we deem this a more reliable approach than others previously applied in the case of a large statistical population like that offered by the VIMS data (more than 100 pixel samples in each cube). In the RADAR parameters considered here, we assign an instrumental error of 0.001 also to the backscattering coefficient σ_0, while when the antenna temperature is included in

the classification, the typical instrumental error associated with it is significantly higher, ranging from 1 to 2 (i.e., 1–2 K).

6. Data analysis

6.1. Medium resolution data

6.1.1. Cube CM_1481607233_1

The first test involved the cube CM_1481607233_1, acquired by VIMS on 13 December 2004 during the Tb flyby (sequence S06, subsequence EUVFUV004) from about 129,000 km in high-resolution IFOV mode, with an IR integration time of 160 ms/pixel and an average phase angle of 15.308°. Because in high-resolution mode the VIMS-IR's IFOV has a rectangular shape, here the average spatial resolution is 60.769 × 121.538 km/pixel.

Fig. 3 shows a RGB image of this cube in the infrared wavelengths. In this case, the data set consists of 3312 VIMS pixels, overlapped with RADAR passes T4, T8, T13 and T16 and showing an average solar incidence angle of 31.671° and an average emission angle of 28.536°. In order to compose the input file to be classified, we consider as variables the reflectances I/F measured by VIMS in the atmospheric windows of the near-infrared spectral region longward of 2 μm, i.e. those centered at the wavelengths of 2.02, 2.69, 2.78 and 5 μm (the latter being an average of 14 spectral channels), combined with the backscattering coefficient σ_0, corrected for the incidence angle, as found in the RADAR SBDR files. Therefore, the data set is made up of 3312 observations in five variables.
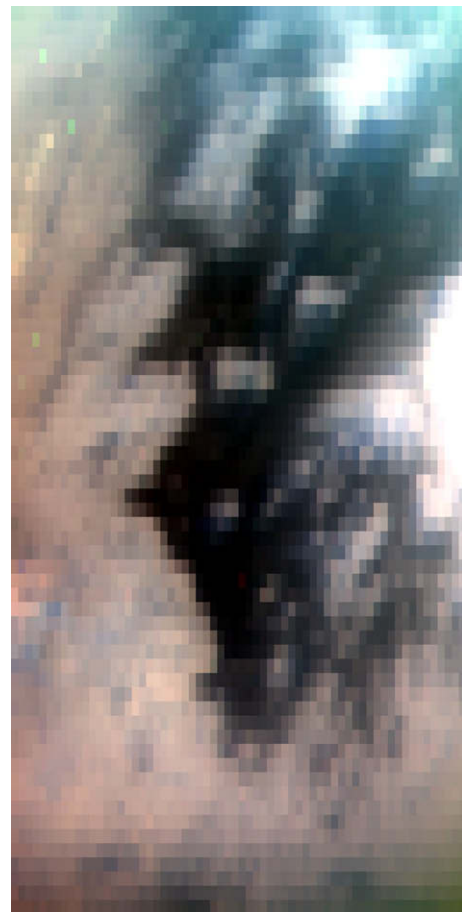
Fig. 3. RGB image ($R = 2.02$ μm, $G = 1.59$ μm, $B = 1.28$ μm) of the VIMS cube CM_1481607233_1, flyby Tb, sequence S06. The average spatial resolution is 60.769 × 121.538 km/pixel, while the average phase angle is 15.308°.

The result of the classification made by applying an instrumental error of 0.001 to all of the variables and a 93.64% confidence level gives 28 homogeneous types, of which here we only show the first 9 for clarity.

Averages for the values of the five variables are shown in Fig. 4a, while statistical weights are shown in Fig. 4b. Such values are rather concentrated in the spectrophotometric variables, while the normalized backscatter cross-section has a larger spread. Type 1 (in red) numbers the most samples (1597 in all) and it is characterized by a low I/F value in all the methane windows (<0.022), coupled to a low (0.15) backscattering coefficient. Type 2 (in blue), consisting of 763 samples, shows I/F values larger than those of type 1 in every atmospheric window, associated with a medium (0.25) scatterometric value. Type 3 (green), with its 178 samples, shows low I/F values in the 2.02 μm atmospheric window, medium values in all the other windows and an average σ_0 value slightly higher (0.287) than in type 2.

It should be noted that carbon dioxide (CO_2) ice was suggested to be present on the surface of Titan both from Earth-based spectroscopy (e.g., Coustenis et al., 2006) and from the VIMS data acquired after the Cassini arrival at Saturn (e.g. Barnes et al., 2005; McCord et al., 2007). Finally, carbon dioxide was tentatively identified by the GCMS onboard the Huygens probe at the landing site (Niemann et al., 2005). At the same time, the dielectric constant of CO_2 ice (2.2) is included in the range of typical dielectric constants that has been retrieved, from Cassini/RADAR data, for the surface of Titan (Zebker et al., 2008).

Carbon dioxide ice shows diagnostic absorptions at 4.26 μm (stretch ν_3), ~2.70 μm (combination $\nu_1 + \nu_3$) and 2.78 μm (combination $2\nu_2 + \nu_3$), whose strength decrease in this order (e.g., Hansen, 1997): on Titan, the first and most prominent signature is masked by a methane absorption band, but the other two signatures approximately match the double peak of the 2.8 μm methane

window, so the ratio between the I/F measured in the 2.69 and 2.78 μm subwindows and the I/F of other windows (particularly at 2 μm, where both H_2O ice and CO_2 ice show an absorption feature) in principle may be diagnostic of surface CO_2 enrichment.

In this case, in type 3 the 2.69/2.02 μm I/F ratio (0.242) as well as the 2.78/2.02 μm I/F ratio (0.286) may be indicative of a relative CO_2 enrichment. Type 4 (cyan), with 65 samples, is recognizable for its higher reflectance at 2.02 μm (0.13) while it is one of the darkest at 5 μm (0.0265), and the σ_0 value is relatively high (0.297). On the other hand, the 2.69/2.02 μm I/F ratio and the 2.78/2.02 μm I/F ratio are the lowest of this classification. Type 5 (ochre yellow) includes only 11 samples, characterized by medium I/F values coupled to a rather low value of the backscattering coefficient σ_0 (0.12). Type 6 (orange), numbering 18 samples, has a medium I/F value at 2.02 μm (0.11), while the reflectance values in the other methane windows (particularly at 5 μm) are among the lowest (0.019) and, on the other hand, the average σ_0 value (0.337) is among the highest of this classification. Type 7 (light cyan), having 56 samples, shows a relatively high reflectance I/F in the windows at 2.02, 2.69 and 2.78 μm, accompanied by a relatively low σ_0 value (0.19). Type 8, with 117 samples, is particularly bright in the 2.69, 2.78 and 5 μm wavelengths, along with the lowest average value of the backscattering coefficient in this cube (0.11). This type also shows the highest value of the ratio 2.69/2.02 μm I/F (0.254) of this classification, consistent with the 2.78/2.02 μm I/F ratio (0.302): this evidence is likely related to composition, particularly the abundance of CO_2 mixtures. Finally, type 9 is by far one of the most peculiar, since it shows high reflectances in all the methane windows combined to a σ_0 average value which is the highest (0.615) found in this work.

Since we keep the geographic information of every sample (pixel), it is possible to estimate the spatial distribution of the nine homogeneous types found by the G-mode by superimposing the
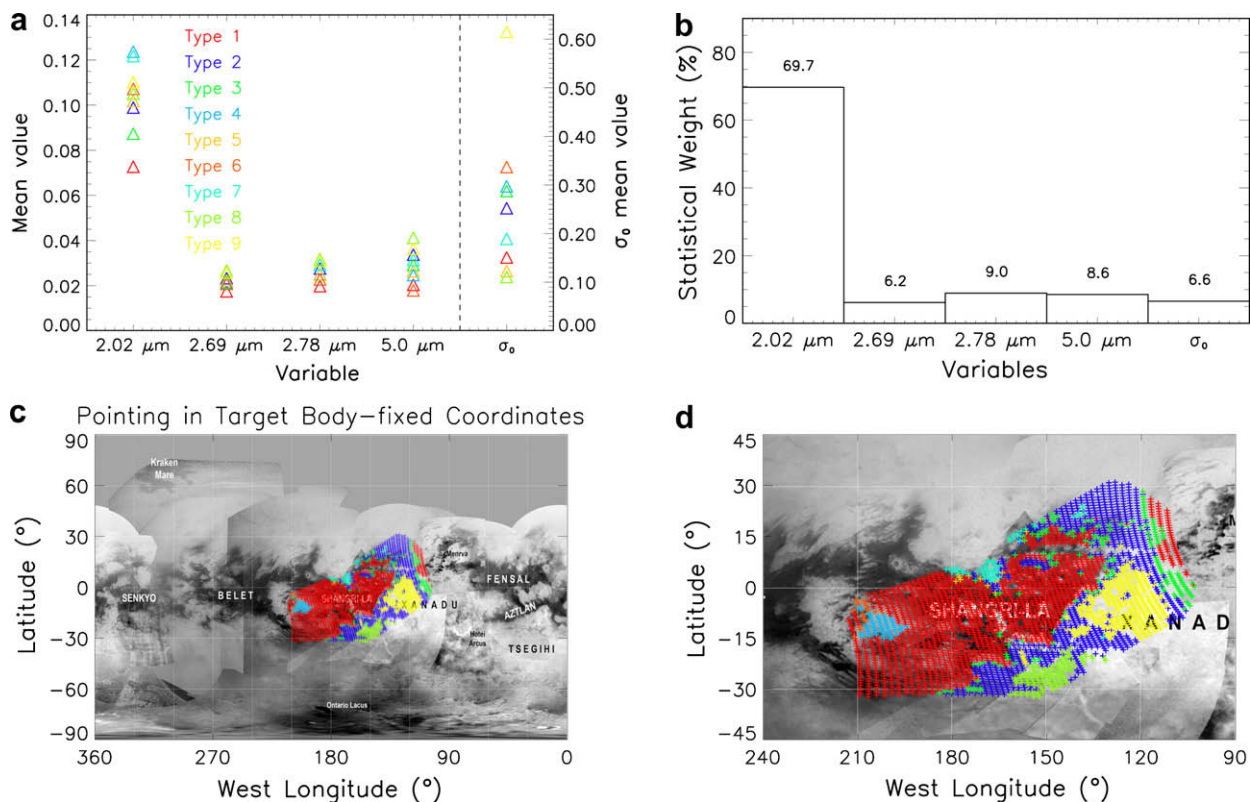
Fig. 4. Classification of cube CM_1481607233_1 with five variables. (a) Mean values of the variables for the nine types identified by the G-mode analysis; (b) statistical weights of the variables; (c) spatial distribution of the samples superimposed to an ISS optical mosaic; (d) magnification of the spatial distribution of samples.

results on a map of Titan's surface on the basis of the best images acquired by ISS with its infrared filter centered at 0.938 μm (Turtle et al., 2009), a methane window where the main geophysical features of the satellite can be highlighted under proper illumination conditions (see Fig. 4c and d). Type 1 (red), the largest, is clearly related to the Shangri-La dark equatorial basin, also including some island-shaped bright features (faculae) within the basin, except for Shikoku Facula. Moreover, some samples from type 1 belong to the eastern border of the cube's image, also corresponding to a dark area (not well recognized in the optical mosaic) probably representing the western border of the Fensal dark equatorial basin. Type 2 (blue) is instead related to the bright features of the southern and eastern areas explored by this cube; it particularly matches the eastern and northern portion of the Xanadu bright continental feature. Type 3 (green) is not concentrated in a single zone, but rather scattered in several regions of the image, and it looks mostly related to some shorelines, i.e. the borders of the bright features degrading towards the Shangri-La and Fensal dark basins. Type 4 (cyan) is related to the brightest portion of the Adiri western feature. Type 5 (ochre yellow) consists of a few samples connected to the southern border of the Dilmun bright feature; type 6 (orange) is also related to the Adiri's inner portion. Type 7 (light cyan) matches the innermost portion of the Dilmun bright feature, while type 8 (light green) is concentrated in the southwestern border of Xanadu and it is brighter than the overall Xanadu physiographic region. Finally, type 9 (yellow) matches the central portion of Xanadu.

It is quite clear that the homogeneous types identified by the G-mode analysis represent rather well regions of Titan that include both dark (types 1 and 3) and bright terrains (types 2, 4, and 7–9). Types 1 and 2 are the main and larger classes of samples, essentially representative of intermediate conditions found in large fractions of the surface (dark equatorial basins and bright features, respectively), though from these "background" trends we can discriminate other minor units, characterized by peculiar behaviors of some variables. In the analyzed VIMS cube, one of the most significant examples in this sense is provided by the Xanadu bright continental feature, having a high backscattering coefficient σ_0 that reaches its top values (>0.9) in the innermost region. On the other hand, the Adiri western bright region shows an interestingly high reflectance – particularly in the 2.02 μm window – associated with a backscattering coefficient σ_0 also having high values (especially in its internal portion), although lower than those detected on Xanadu. In the northern hemisphere, the Dilmun bright region also shows a high I/F at 2.02 μm, but the backscattering coefficient is not as high as the value found in Xanadu and Adiri. As regards the dark regions, here we have a smaller variety of behaviors, although the existence of some small homogeneous types related to the shorelines of Shangri-La, as well as the evidence that most faculae appearing in the Shangri-La basin are classified in the same type of dark terrains, suggests that the transition between bright features and dark basins is smooth rather than sharp.

In order to test if and how the results are affected by a different combination of variables, we have repeated the classification including the calibrated antenna temperature measured along with the scatterometry echoes at an average emission angle of 31.750°, and removing the spectrophotometric variables represented by the I/Fs measured at 2.02, 2.69 and 2.78 μm. In this way, the data set to be classified now consists of 3312 samples, each depending on three variables (respectively I/F at 5 μm, σ_0 and T_a). This simple approach is also interesting to evaluate how Titan's surface is classified with respect to three different physical parameters.

By applying the G-mode with an instrumental error of 0.001, except the temperature variable where, because of the higher uncertainty affecting the measurements, a 1.0 error value (i.e.

1 K error) is assigned, and with a 87% confidence level, the processing returns five homogeneous types. The average values of these variables are revealed in Fig. 5a with a color code related to the temperature (the antenna temperature itself is scaled by a factor of 10^2 to allow a better visualization), while statistical weights are represented in Fig. 5b. With this combination of parameters, the leading variable is the backscattering coefficient σ_0; nevertheless the information provided by the 5 μm reflectivity and by the antenna temperature have a very similar weight, which is also relevant in the classification. By checking the spatial distribution of the homogeneous types (Fig. 5c and d), it turns out that type 1 (red), consisting of 973 samples, is characterized by a low backscattering coefficient value (0.11) and a relatively high antenna temperature (95.5 K); it matches rather well the dark terrains seen in the optical mosaic. Type 2 (ochre yellow), numbering 928 samples, shows intermediate characteristics between the dark and bright terrains: it has a medium reflectance (0.032) at 5 μm, relatively low backscattering coefficient (0.18) and a medium temperature (~3 K lower than in type 1). This type is especially related to an area located southwest of Xanadu beyond the Tui Regio, to a large fraction of terrain north of Xanadu and east of Dilmun; and also to the southern border of Dilmun and the eastern boundary of Adiri. Types 3 and 4 (green and cyan, respectively) include a few samples with low I/F (<0.03) at 5 μm, medium temperature (~3 K lower than in type 1) and a medium backscattering coefficient (0.30–0.27), not related to any defined structure. Type 5 (blue), the largest type with its 1305 samples, shows the highest I/F (0.034) at 5 μm, the highest average backscattering coefficient (0.37) and the lowest temperature (more than 7 K lower than the temperature measured in the dark basins and more than 4 K lower than the average temperature of type 2). This type is clearly related to the Xanadu continental region and partly to the Adiri bright feature.

In summary, by using only three variables and including the antenna temperature among these, the boundaries traced by the homogeneous types on the surface of Titan change. The classification becomes less detailed with respect to the use of five variables, but a general distinction between the dark equatorial basins and the regional bright features is preserved. In particular, the similarity between the Xanadu region and the norther portion of Adiri is maintained also on the radiometry side (general lower temperature), while the Dilmun bright feature belongs to a distinct type representing an intermediate condition. Moreover, the addition of the antenna temperature reveals a patchy structure in the Shangri-La basin, with the south-eastern part of Adiri emerging from an otherwise uniform background.

At microwave frequencies, regions appear dark if they are smooth, if they are sloped away from the direction of illumination, if they are made of microwave-absorbing materials, or for a combination of these causes. Conversely, regions will appear microwave-bright if they are of rougher terrain, if they have slopes facing the radar, if they are made of more reflective materials, if significant volume scattering is present, or for a combination of these causes (Wye et al., 2007). From the joint analysis of the RADAR scatterometry and radiometry data, Titan surface dielectric constants do not span a wide range, most values being comprised between 1.75 and 2.5, compatible with simple ices and liquid/solid hydrocarbons (Janssen et al., 2006, 2009a; Zebker et al., 2008). From both classifications performed on this cube, we can infer that the optically dark equatorial basins, appearing dark also at near-infrared wavelengths, likely consist of a kind of terrain rather smooth and/or filled of microwave-absorbing material (in principle, these regions could appear dark also because they are sloped away from the direction of illumination, but examination of a wide range of incidence angles militates against this eventuality), presumably rich in heavy hydrocarbons
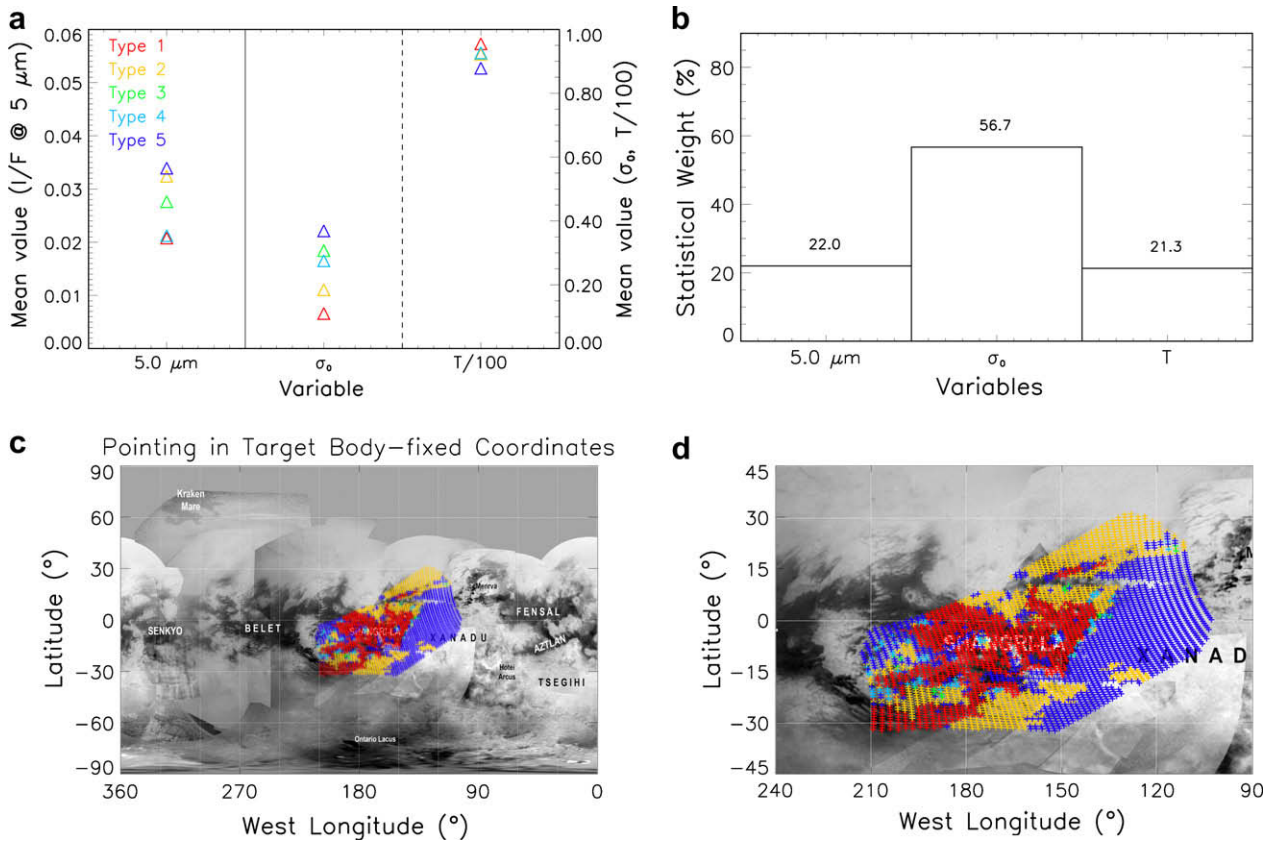
Fig. 5. Classification of cube CM_1481607233_1 with three variables, including antenna temperature. (a) Mean values of the variables for the five types identified by the *G*-mode analysis; (b) statistical weights of the variables; (c) spatial distribution of the samples superimposed to an ISS optical mosaic; (d) magnification of the spatial distribution of samples.

and/or nitriles precipitated from the atmosphere. Dark basins also correspond to the warmest regions of the satellite, consistently with the higher emissivity of this material (Janssen et al., 2009a). These results are also in accordance with the brightness surface temperatures derived from the spectral analysis of data returned by the Composite Infrared Spectrometer (CIRS) (Jennings et al., 2009), which produced a large amount of spectra during the Cassini's 4-years nominal mission, and with the in situ temperature measurements of the Huygens Atmospheric Structure Instrument (HASI) (Fulchignoni et al., 2005).

The Xanadu bright region shows a surprisingly high backscattering coefficient, reaching top values in its central region. Since in the RADAR passes considered in this work (particularly in T8 which had the best chance to observe this region in the scatterometry mode), this feature is observed at intermediate incidence angles, we can exclude that this is due to a preferential orientation of the topography with respect to the incident beam. Therefore, the Xanadu feature is microwave-bright because it shows a prominent roughness on a regional scale and/or because it possesses a large volume-scattering effect. The latter effect is in agreement with the lower antenna temperature characterizing this feature, consistent with a porous structure of the surface material (Janssen et al., 2009a,b). On the other hand, this behavior is not seen on the southwestern border of Xanadu located beyond the Tui Regio (the brightest spot on Titan at 5 μm), showing a relatively low σ_0 value measured at low incidence angles and a medium antenna temperature: here the data are rather consistent with a moderate surface roughness (possibly combined with a different dielectric constant), or at least with a physical situation where the volume scattering is not prominent.

6.1.2. Cube CM_1514287583_1

As a second test on medium resolution data, the *G*-mode was applied on the cube CM_1514287583_1, acquired on 26 December 2005 during the T9 flyby (sequence S17, subsequence MEDRES001) from a distance of about 156,271 km in nominal IFOV mode, with an IR integration time of 160 ms/pixel, an average phase angle of 27.693° and an average spatial resolution of 73.941 km/pixel.

Fig. 6 shows a RGB image of this cube in the near-infrared, where both bright and dark features can be seen. In this case, the data set is made up of 405 VIMS pixels, overlapping with the T3 scatterometric pass, with an average solar incidence angle of 40.536° and an average emission angle of 27.374°. Here we considered three spectrophotometric variables, centered at 2.69, 2.78 and 5 μm respectively, plus the normalized backscatter cross-section σ_0 and the calibrated antenna temperature (whose emission angle in this pass spans a wide range of values, the average value being 34.182°), so the array to be classified consists of 405 samples in five variables. The 2.02 μm window was not included on purpose in this classification: since this variable had the largest statistical weight in the classification performed in the previous cube and shown in Fig. 4, we omitted it from this test in order to emphasize the role of the other variables and see how the classification is driven by them.

In this case, by reapplying the *G*-mode with a 98.42% confidence level and an instrumental error of 0.001 for all the variables except for the temperature, where an error of 1.400 (i.e. 1.4 K) looks more appropriate, the classification returns nine homogeneous types, whose average variables' values and relative weights are represented in Fig. 7a and b.
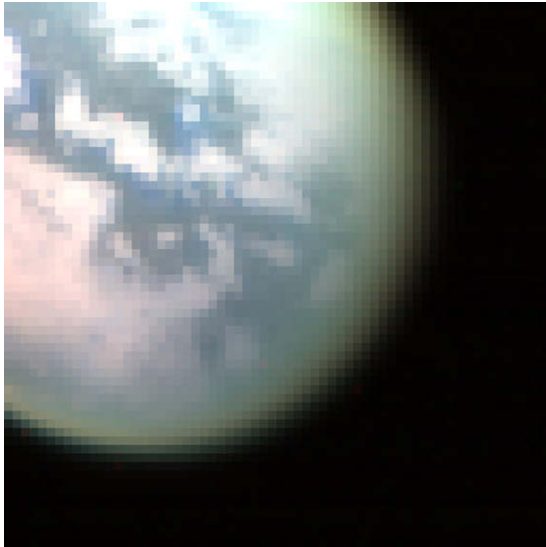
Fig. 6. RGB image ($R = 2.02$ μm, $G = 1.59$ μm, $B = 1.28$ μm) of the VIMS cube CM_1514287583_1, flyby T9, sequence S17. The average spatial resolution is 73.941 km/pixel, while the average phase angle is 27.693°.

By superimposing these homogeneous types on the ISS optical mosaic (Fig. 7c and d), it is possible to inspect their spatial distribution. The few samples of type 2 (light green) at the northernmost latitudes analyzed here have the highest average backscattering coefficient's value of this RADAR pass (0.20), while maintaining a temperature similar to that of the surrounding samples of type 1

(yellow). This matches a bright terrain (partly including the Quivira feature, centered on the equator) dividing the two dark basins Aaru and Fensal. On the other hand, samples of type 7 (green), matching the Tsegihi bright feature in the southernmost explored latitudes, show the highest reflectances at 2.69, 2.78 and 5 μm, while having a medium–low backscattering value and an average antenna temperature ~5 K lower than the warmer types 4 and 6 (red and orange, respectively). These types are made up of a few samples well overlapping an inlet of the Atzlan dark equatorial basin on the border of Tsegihi, also showing relatively low values of reflectance and backscattering. Type 3 (ochre yellow) shows the lowest reflectances in all of the sampled methane windows, a low σ_0 value (0.117) and a relatively high antenna temperature (94.4 K): this homogeneous type matches a sizable portion of the dark terrains explored by this RADAR pass and recognizable in the ISS images (the emission angle reaches its minimum right near the equator, so the radiometric parameter in this region is more reliable). Finally, type 8 (cyan), characterized by a relatively high average reflectance at 5 μm (0.035) and a medium backscattering coefficient (0.15), shows a low antenna temperature (4–5 K lower than in types 3, 4 and 6).

6.2. Medium–high resolution data

6.2.1. Cube CM_1477490933_1

As a third test, the G-mode method has been applied to the cube CM_1477490933_1, acquired by VIMS on 26 October 2004 during the Ta flyby (sequence S05, subsequence TRANS003) from a distance of 31,843 km in nominal IFOV mode, with a IR integration time of 200 ms/pixel, an average phase angle of 12.731° and an
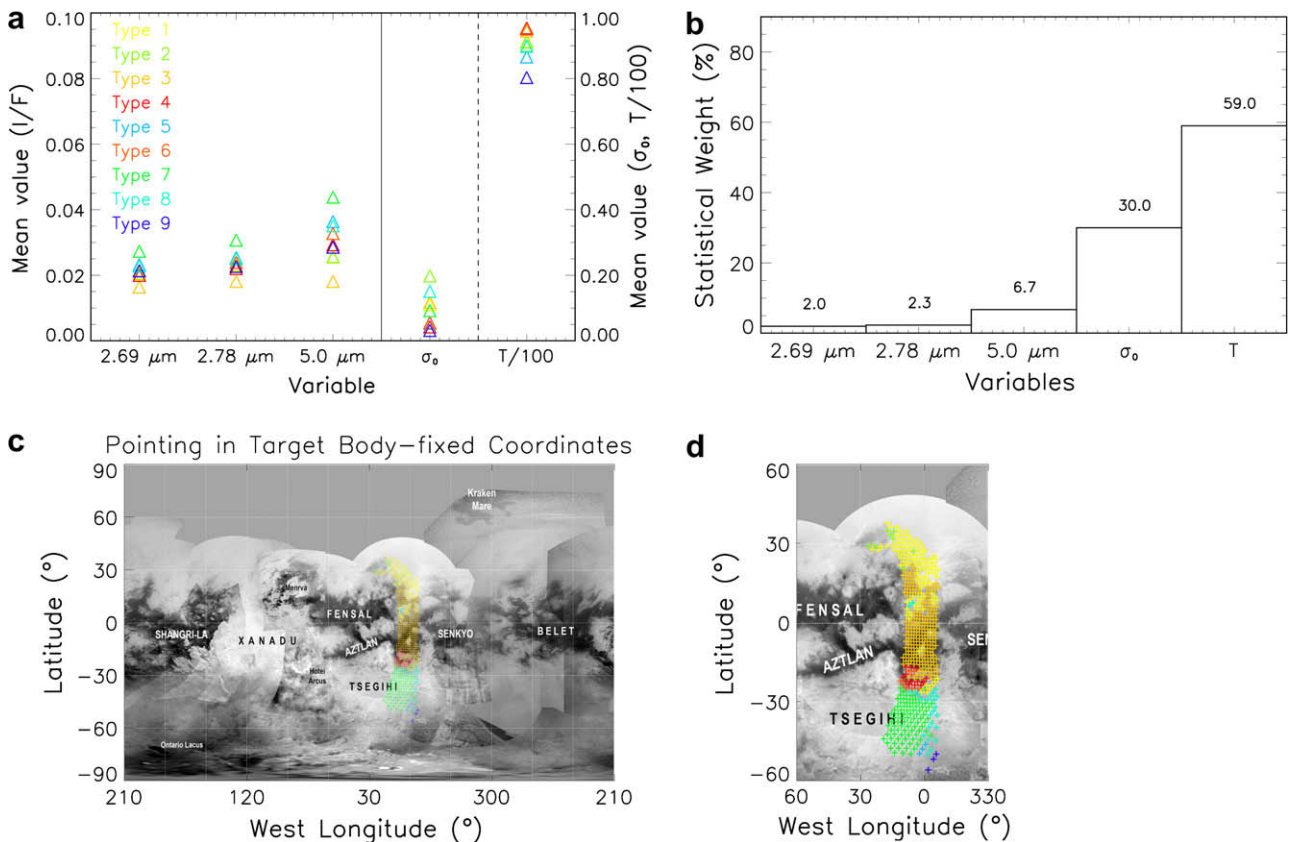
Fig. 7. Classification of cube CM_1514287583_1 with five variables, including antenna temperature. (a) Mean values of the variables for the nine types identified by the G-mode analysis; (b) statistical weights of the variables; (c) spatial distribution of the samples superimposed to an ISS optical mosaic; (d) magnification of the spatial distribution of samples.

Fig. 8. RGB image ($R = 2.02$ μm, $G = 1.59$ μm, $B = 1.28$ μm) of the VIMS cube CM_1477490933_1, flyby Ta, sequence S05. The spatial resolution is 15.140 km/pixel, while the average phase angle is 12.731°. The bright features seen in the image appear warped due to a spacecraft's motion during the acquisition.

average spatial resolution of 15.140 km/pixel. The above subsequence includes a couple of cubes, looking approximately at the same region and acquired 15 min from each other, before the closest approach; however the second of these cubes was discarded because it was acquired with a lower exposure time. Fig. 8 shows a RGB image of this cube in the infrared.

With its 4004 pixels overlapping with the RADAR scatterometry footprints from flybys T8 and T13, this is the cube exhibiting, in the VIMS data set considered here, the largest number of samples for the classification. This cube, showing an average solar incidence angle of 35.921° and an average emission angle of 30.711°, was also used by Rodriguez et al. (2006) to characterize the Huygens landing site (Lon. 192.5°W, Lat. 10.5°S) and surrounding terrains by evaluating spectral ratios in several atmospheric windows in the near-infrared.

Because the spacecraft moved during the acquisition of this cube, the image features appear warped, but thanks to the ISIS software, based on the standard SPICE system and using the latest available products reconstructed *a posteriori* for the spacecraft's trajectory and attitude, it is possible to accurately determine the geometry of all the pixels' centroids. We initially considered only the variables related to the four VIMS reflectances measured in as many atmospheric windows from 2 to 5 μm, combined with the scatterometry parameter, so that the matrix to be classified consists of 4004 samples in five variables.

The G-mode method has been initially applied by considering an identical instrumental error of 0.001 for all of the variables, in order not to influence *a priori* the trend of statistical weights in the processing. By assuming for this test a confidence level of 95.3%, the classification returns nine homogeneous types, the first being the largest with 2163 samples, while the other types have 1215, 456, 19, 22, 67, 13, 5, and 4 samples, respectively. From Fig. 9a, showing the average values of the variables for the nine homogeneous types identified by the G-mode, it can be noted that the fifth variable, namely the normalized backscatter cross-section σ_0, clearly shows the largest spread.

With reference to the first and the second types, characterized by a larger number of samples, one can see that type 1 (in red)
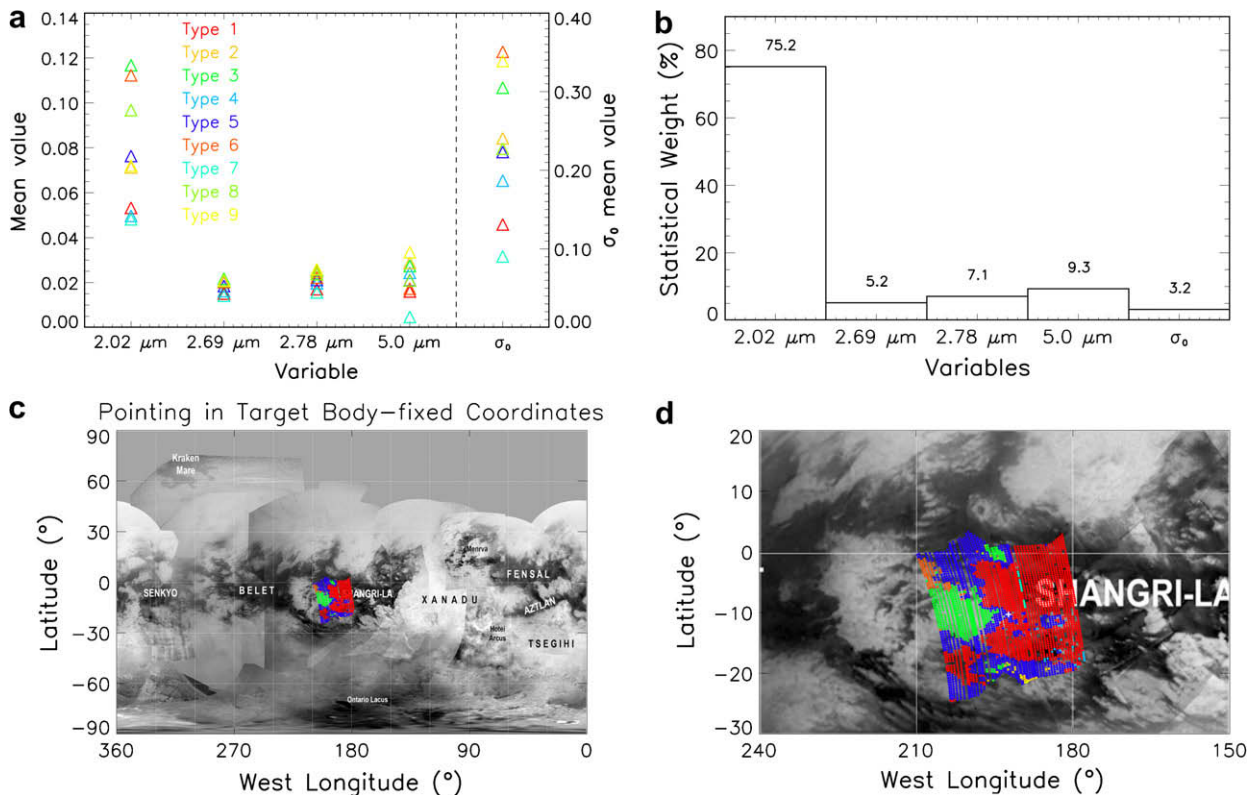
Fig. 9. Classification of cube CM_1477490933_1 with five variables. (a) Mean values of the variables for the nine types identified by the G-mode analysis; (b) statistical weights of the variables; (c) spatial distribution of the samples superimposed to an ISS optical mosaic; (d) magnification of the spatial distribution of samples. The estimated position of the Huygens landing site is indicated by a white cross.

shows rather low average values of the spectrophotometric variables (i.e., reflectances I/F) and of the normalized backscatter cross-section σ_0 (0.13). Type 2 (ochre yellow) has the peculiarity of having a low I/F at 2.02 μm (0.076), while it has higher values of all the other variables. Type 3 (green), shows relatively high values of all the five variables (particularly the reflectance at 2.02 μm: 0.125), and low values of the 2.69/2.02 and 2.78/2.02 μm I/F ratios (0.19 and 0.22, respectively), possibly related to composition. Type 4 (cyan) is related to low values of the spectrophotometric variables and it shows a medium σ_0 value (0.187); this type also exhibits the highest values of the 2.69/2.02 μm I/F ratio (0.326) and 2.78/2.02 μm I/F ratio (0.396), possibly indicative of an enrichment in CO_2 ice. Type 5 (blue) is prominent, and it shows intermediate values on the basis of all the variables. Type 6 (orange) is peculiar, being characterized by a relatively high I/F in the 2.02 μm window (0.12) and the highest backscatter coefficient found in this classification (0.35), while the I/F at 5 μm is almost as low as in type 1 (0.018) and the low 2.69/2.02 and 2.78/2.02 μm I/F ratios (0.18 and 0.20, respectively) may be indicative of a depletion of CO_2. Type 7 (light cyan) is characterized by the lowest values of all the variables, type 8 (light green) again has intermediate values for all the variables, and finally type 9 (yellow) has a low value of the 2.02 μm reflectance, with the other variables reaching the highest values.

The spatial distribution of the homogeneous types can be evaluated by superimposing the samples on the mosaic coming from optical images (see Fig. 9c, magnified in Fig. 9d); on this point it should be noted that most pixels of this VIMS cube overlap with the T8 scatterometric pass, while in the southern portion some samples overlap flyby T13.

Type 1 (in red) embraces the western portion of the Shangri-La dark equatorial basin, while type 3 (green) largely overlaps with the eastern border of the Adiri bright feature (in between the two Belet and Shangri-La dark basins), and type 5 (blue) covers an intermediate zone between these two types, also including the Huygens landing site. The other types consist of a smaller amount of samples, with the exception of type 6 (orange), also related to the eastern border of Adiri. Interestingly enough, some of the results are consistent with the geological map described in Rodriguez et al. (2006): type 3 is mostly related to bright material and largely matches the light yellow unit found in Fig. 11 of their work, while type 1 is related to the dark terrain and largely matches the brown and light brown units (dark mottled material and bright diffuse material, respectively) of the same map. However, our classification is performed on a subset of methane windows with $\lambda > 2$ μm and it is driven not only by the spectral behavior, but also by the scatterometry (and antenna temperature when appropriate), so that albedo-correlated, peculiar spectral units can get lost while correlations with topography and volume scattering effects stand out. The Huygens landing site has been interpreted to be enriched in water ice due to its lower reflectivity in the 1.59 and 2.02 μm windows (Tomasko et al., 2005; Rodriguez

et al., 2006; Soderblom et al., 2007); GCMS data suggest that the soil at the site is suffused with volatile hydrocarbons and nitriles, and possibly carbon dioxide (Niemann et al., 2005). It is a possible, but not necessary, interpretation that these materials are responsible for the lowered reflectivity interpreted to be water ice, since certain organics or a combination of organics can mimic the water ice signature centered at 1.5 μm. In our classification, this site is included in type 5, showing intermediate characteristics between the bright and dark terrains on the basis of all variables.

From this classification, we can draw the following conclusions. The two main homogeneous types, i.e. types 1 and 5, correspond to two "average" or "background" situations on the basis of all the examined variables (type 1 darker and with a lower backscattering coefficient, type 5 brighter and with a higher σ_0 value). With respect to these two main classes, other smaller homogeneous types are characterized by a significantly stronger value of some of the variables. For example, type 3 is the brightest in the 2.02 and 2.69 μm; type 6 is very bright at 2.02 μm and shows the highest σ_0 value; type 9 is the brightest at 2.78 and 5 μm and also shows a high σ_0 value; while type 7 is by far the darkest and smoothest, on the basis of all variables.

The distance matrix is computed by the G-mode at the end of the processing (see Table 5) and it represents the statistical (Euclidean) distances of each homogeneous type with respect to the others in the multidimensional space of the variables. Hence large values in this matrix are indicative of homogeneous types that are significantly different from each other on the basis of all the meaningful variables, while small values are indicative of taxonomic units similar to each other. In this case, the distance matrix shows that the major differences exist between types 3 and 9, and between types 7 and 9. Moreover, the statistical weights computed by the G-mode after all the homogeneous types have been found (Fig. 9b) show how in this classification the leading variable is the reflectance I/F measured by VIMS at 2.02 μm, a wavelength which is also characterized by a fair instrumental SNR.

On this point, it is interesting to note how, by removing this variable, the classification remains essentially unchanged: if we consider a data set of 4004 samples in 4 variables instead of 5, by applying always an instrumental error of 0.001 to all the variables and a 96.2% confidence level, the classification returns nine homogeneous types. In this case, type 2 again has a number of samples larger than type 1 on the basis of all the variables; however it includes almost all the samples that in the previous classification were numbered in type 3, and again it includes the Huygens landing site, while types 3 and 5, matching previous types 6 and 7, still maintain their identity. In this new classification, type 4 consists of 50 samples characterized by high I/F values in all of the spectrophotometric variables and a high σ_0 backscattering coefficient value. Finally, the statistical weights show that in this classification the leading variable is the σ_0 backscattering coefficient.

From this result, it is possible to infer that the classification is rather stable, not conditioned by the use of a specific variable:

Table 5
Square root of the distance matrix computed by the G-mode for the classification of cube CM_1477490933_1.

	Type 1	Type 2	Type 3	Type 4	Type 5	Type 6	Type 7	Type 8	Type 9
Type 1	1.00	3.14	6.41	5.55	7.92	7.21	5.04	21.17	14.77
Type 2	3.14	1.00	4.22	5.19	5.80	5.25	9.55	15.40	10.76
Type 3	6.41	4.22	1.00	8.91	4.85	3.20	17.89	10.92	20.34
Type 4	5.55	5.19	8.91	1.00	6.95	7.97	15.33	7.30	17.56
Type 5	7.92	5.80	4.85	6.95	1.00	4.54	14.91	6.99	18.00
Type 6	7.21	5.25	3.20	7.97	4.54	1.00	15.83	7.05	18.57
Type 7	5.04	9.55	17.89	15.33	14.91	15.83	1.00	10.10	18.74
Type 8	21.17	15.40	10.92	7.30	6.99	7.05	10.10	1.00	17.59
Type 9	14.77	10.76	20.34	17.56	18.00	18.57	18.74	17.59	1.00

the main and most significant homogeneous types, related to different standard condition of the surface of Titan, remain essentially unchanged. An exception is represented by type 3 (green) of the five-variables classification, which tends to merge with type 2 if the 2.02 μm I/F is not considered: this means that type 3, partly corresponding to the Adiri bright region, is particularly notable for its high reflectance at that wavelength.

In general, in this classification one can see that regions which are darker on the spectrophotometric side also correspond to a lower σ_0 backscattering coefficient value, while the bright features have a higher backscattering value; although some types, consisting of a few pixels, do not follow this trend (particularly with respect to the 2.02 μm reflectance). For this reason, we can infer that dark dune fields are smooth on a regional scale, and they are mantled with a material, presumably rich in complex hydrocarbons and/or nitriles, where the volume scattering is not relevant. The Huygens landing site, located on the northeastern border of the Adiri bright feature declining towards the Shangri-La dark basin, is consistently grouped in one of the major homogeneous types (type 2, in blue), representing a transitional condition between bright and dark terrains on the basis of all the considered variables.

6.3. High resolution data

6.3.1. Cube CM_1477495058_1

A fourth and last test was performed on cube CM_14 77495058_1, acquired by VIMS on 26 October 2004 during the Ta flyby (sequence S05, subsequence HIRES002) from a distance of about 8248 km in nominal IFOV mode, with an IR integration time of 240 ms/pixel, an average phase angle of 19.620° and an average spatial resolution of 3.942 km/pixel. Like in the case of cube CM_1477490933_1, this subsequence includes two cubes looking at the same region, acquired by VIMS with an interval of 18 min between each other and prior to the closest approach; but the second cube was discarded due to its low exposure time. Fig. 10 shows a RGB image of this cube in the infrared portion of its spectrum.

Because the spacecraft was moving at 5.8 km s^{-1} with respect to the target while approaching the minimum distance point, it
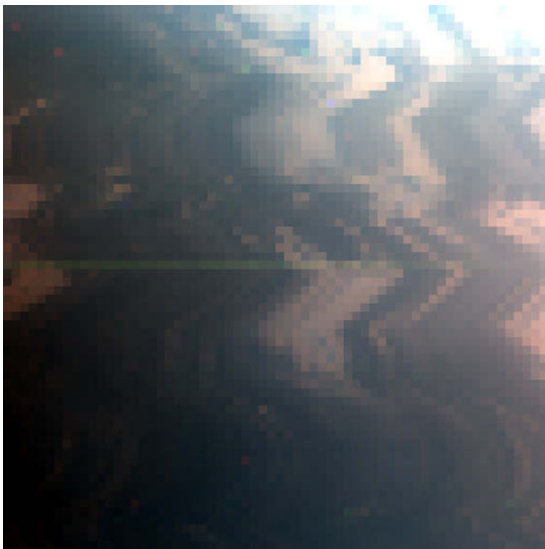
Fig. 10. RGB image (R = 2.02 μm, G = 1.59 μm, B = 1.28 μm) of the VIMS cube CM_1477490958_1, flyby Ta, sequence S05. The spatial resolution is 3.942 km/pixel, while the average phase angle is 19.620°. The bright features seen in the image (among which Tortola Facula) appear warped due to a spacecraft's attitude slew during the acquisition.

was necessary to slew its attitude in order to keep the pointing direction fixed on the same zone. Since VIMS was acquiring during this maneuver, the framed details appear warped, but through the ISIS software it is possible to retrieve an accurate geometric information for every pixel. In this case, the data set consists of 2842 VIMS pixels, overlapping the T8 scatterometric pass, representing a relatively small portion of the surface of Titan and indicative of the geophysics of the satellite at a high resolution. These pixels show an average solar incidence angle of 33.980° and an average emission angle of 16.220°. As usual, the classification begins by considering five standard variables (I/F reflectances at 2.02, 2.69, 2.78 and 5 μm, plus the backscattering coefficient corrected for the incidence angle). By applying an identical instrumental error of 0.001 to all of the variables, with a 99.24% confidence level, the G-mode returns four homogeneous types, the first type being the largest with 2570 samples, while the other types have 187, 71 and 4 samples respectively. Fig. 11a shows the average values of the variable for these four types. First of all, one can see that, among the spectrophotometric variables, the I/F at 2.02 μm shows the larger spread, while the other spectrophotometric variables (I/Fs at 2.69, 2.78 and 5 μm) show average values more concentrated among the different types. The analysis of the statistical weights computed at the end of the processing (Fig. 11b) reveals that, in this classification, the most prominent variable is the reflectance measured at 2.02 μm followed by the backscattering coefficient σ_0, while the other variables have a minor weight.

In this case, type 3 (green) has the highest reflectance in the windows centered at 2.02, 2.69 and 2.78 μm and a higher normalized backscatter cross-section (0.325), while type 4 (cyan) has the same backscatter cross-section while showing the lowest reflectance I/F at 5 μm. Type 2 (blue) shows the highest reflectance at 5 μm, while the average backscattering coefficient is low (0.187). Type 1 (red), the largest, has the lowest I/F at 2.02, 2.69 and 2.78 μm, and it also shows the lowest average backscattering coefficient.

The analysis of the spatial distribution of the homogeneous types on the optical mosaic of the surface of Titan shows how they are concentrated in the VIMS cube considered here, sometimes tracing the shape of the scatterometry footprints, as would be expected since the scatterometry also has a relevant weight in this classification. Type 1 basically overlaps the northeastern part of the Shangri-La dark basin and is therefore related to dark terrains, but it also includes Tortola Facula and the southern part of Crete Facula. Tortola Facula is a 65-km wide feature (centered at Lon. 143.1°W, Lat. 8.8°N), located almost in the center of the image in Fig. 10, that was suggested as a possible cryovolcanic structure in previous work (Sotin et al., 2005; Soderblom et al., 2005). Type 3 includes the eastern border of Crete Facula, while type 2 sits in the region between Crete Facula and the dark terrain.

Since this cube covers a relatively small portion of surface, here the antenna temperature is less meaningful with respect to the medium resolution case. In fact, by adding this parameter (that in this set of data is measured at an average emission angle of 18.684°) in the classification, we find that the temperature is very homogeneous in the explored region, with the exception of the northeastern border identified by the samples of type 1 related to Tortola Facula, where the antenna temperature is about 1 K less than in the rest of the region (in this point, the emission angle is 19.76°).

Cassini RADAR has provided evidence of cryovolcanic flows and domes on the surface of Titan (Elachi et al., 2005; Lopes et al., 2007). In particular, it has been suggested that the Tortola Facula feature seen in cube CM_1477495058_1 is a cryovolcanic edifice (Sotin et al., 2005). In general, cryovolcanic features are expected to be RADAR-bright (essentially as a consequence of higher dielectric constants in the vicinity of the cryovolcanic caldera, possibly
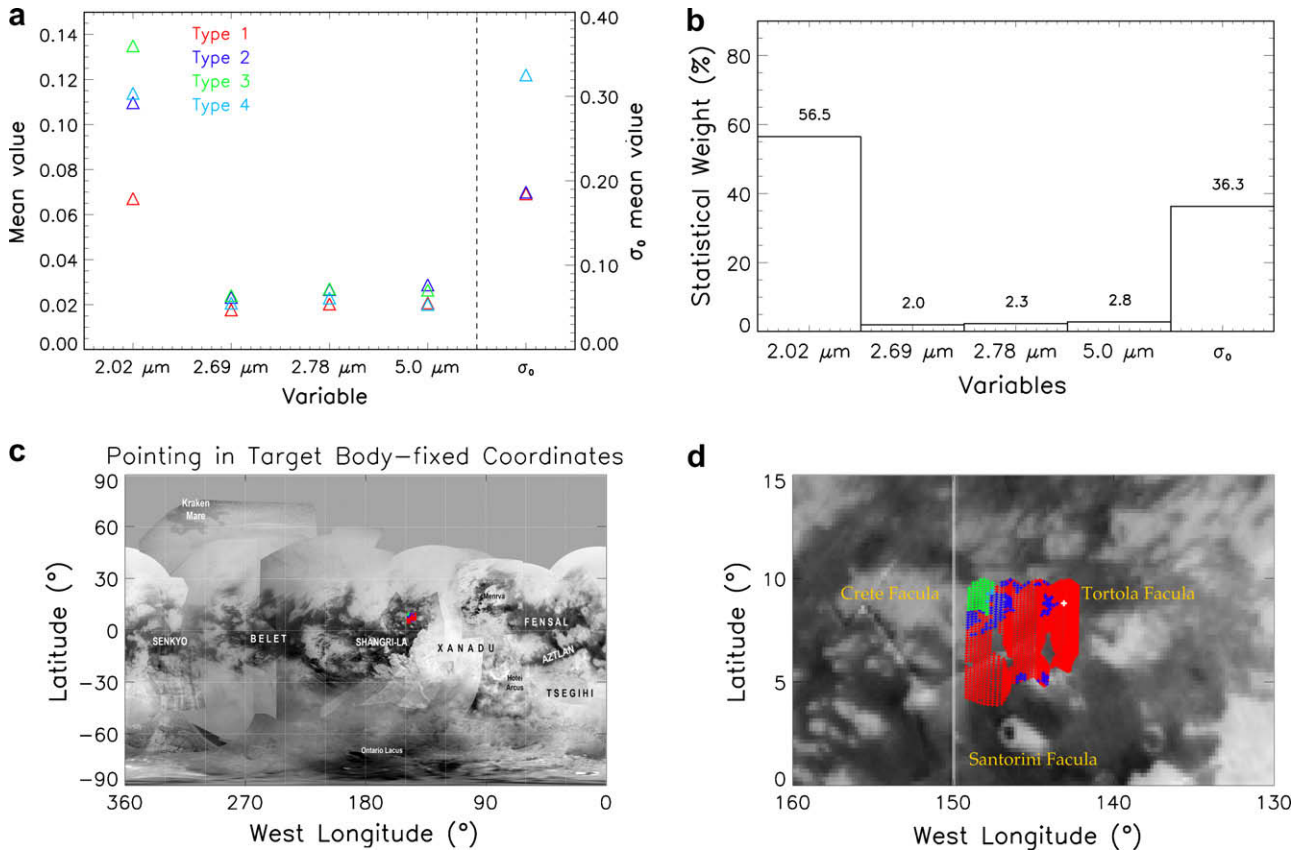
Fig. 11. Classification of cube CM_1477490958_1 with five variables. (a) Mean values of the variables for the 10 types identified by the *G*-mode analysis; (b) statistical weights of the variables; (c) spatial distribution of the samples superimposed to an ISS optical mosaic; (d) magnification of the spatial distribution of samples. The position of Tortola Facula is highlighted by a white cross.

due to water/ammonia ice) and to show a morphology compatible with flows of liquid material; in this sense, high-resolution (down to ∼300 m) SAR images, allowing the analysis of morphology and topography of the presumed cryovolcanic features, are more suited for combination with these higher resolution VIMS data.

However, in the case of this cube, showing the highest spatial resolution among the cases treated here, and with the technique we have used, a cryovolcanic activity would rather expected to be indicated by a peculiar spectral unit, with strong signatures of H_2O ice producing a low reflectivity in the 1.59 and 2.02 μm windows, and/or possibly NH_3 signatures resulting in a drop of the reflectivity at 2.02, 2.69 and 2.78 μm. This may be combined with high reflectance in the 5 μm window due to the thermal emission from the surface (possibly comparable with the brightness of the Tui Regio, see Barnes et al. (2005)), high radar albedo, and with a radiometric temperature significantly greater than the nearby regions; properties that are not seen in this cube and particularly in the samples corresponding to the Tortola Facula feature.

7. Summary and conclusions

From this work, focused on the combination of VIMS and RADAR data of Titan, we can draw some general conclusions. An automatic multivariate method, like the *G*-mode unsupervised clustering method used here, is shown to be essential in order to undertake a complete data analysis when the number of samples or observations dependant on several variables is very high, which is the case of the data acquired by Cassini's remote sensing instruments for Titan and more generally for the Saturn system. The flex-

ibility of the *G*-mode method allows the user to test different types of classification by removing or adding variables and then evaluating their statistical weight, the distance of the homogeneous classes with respect to each other on the basis of all the meaningful variables, and the stability of the classification.

The main scientific conclusions of this analysis are: among the considered variables, we find a larger dispersion in the average values of the reflectance at 2.02 μm and of the backscattering coefficient σ_0. As far as the 2.02 μm window is concerned, when only data with convenient (small) phase and illumination angles are selected so that residual haze scattering effects are safely negligible, this dispersion is likely related to differences in composition. On the other hand, variables showing higher statistical weight are almost always the reflectances measured by VIMS in the methane windows at 2.02 μm and 5 μm, as well as the backscattering coefficient σ_0 and the antenna temperature (to be taken into account preferably for small emission angles, where the lack of a correction for this parameter is less relevant). The two spectrophotometric variables represented by the *I/F*s measured in the double-peaked window at 2.69 and 2.78 μm are less meaningful: here the different homogeneous types show average values very close to each other, as a joint consequence of the low level of radiance and of the larger instrumental noise in this spectral region. However, different *I/F* values in the 2.69 and 2.78 μm windows can be indicative of compositional variability, and the 2.69/2.02 μm and 2.78/2.02 μm *I/F* ratios may be particularly related to the abundance of CO_2 ice on the surface.

In medium resolution data, sampling relatively large portions of the satellite's surface, regional geophysical units matching both the major dark and bright features seen in the optical mosaic are

identified. In particular, given the VIMS and RADAR data used in this work, the largest homogeneous type is associated with the dark equatorial basins, where the dune fields are located. The corresponding pixels show the lowest reflectance levels in all of the sampled atmospheric windows, so these regions appear dark also in the near-infrared range up to 5 μm; they also have a rather low backscattering coefficient (typically <0.15 on an average) that is most likely indicative of surfaces that are relatively smooth on a regional scale. Further, these regions – that are filled with a material whose low dielectric constant is compatible with hydrocarbons and/or nitriles precipitated out of the atmosphere – are not affected by significant volume scattering processes.

In dark basins, the calibrated antenna temperature is, on an average, higher than on the rest of the satellite (reaching the highest values in Shangri-La and Atzlan), consistently with the higher emissivity of the material with which these basins are filled. Furthermore, some small bright features (*faculae*), present within the dark basins, show a behavior not too different from that of the surrounding dark terrains on a regional scale, while they can be distinguished from the background terrain in higher resolution data. At a medium resolution, the Xanadu bright continental feature is one of the most interesting geophysical units of Titan: this region shows the highest backscattering coefficient of the entire satellite (>0.6 on an average). Since this behavior is seen at several incident angles and not only at small incidence angles, we exclude that this is due to the peculiar observational geometry: the Xanadu region is likely to be microwave-bright because it shows a high regional roughness on the scale of the radar wavelength, or because it possesses a significant amount of volume scattering (Janssen et al., 2009a,b).

The antenna temperature of Xanadu, that on an average is 7 K lower than the temperature detected in Shangri-La and more than 4 K lower than the temperature representing more general conditions on the satellite, seems consistent with a porous structure of the composing material, in turn consistent with the above-cited volume-scattering effect (Janssen et al., 2009b). This behavior is also observed in the Adiri western bright feature (setting in between the two Belet and Shangri-La dark basins), that is particularly bright at 2.02 μm and possibly less enriched in CO_2 ice with respect to other bright units (at least in its eastern border). It is not observed in a region located southwest of Xanadu, beyond the Tui Regio, that is bright at 2.69, 2.78 and 5 μm while showing a low σ_0 value measured at small incidence angles and a medium temperature: here the classification returned by the *G*-mode seems to trace the boundaries of a detached geophysical unit, characterized by a low surface roughness or by a condition where the volume scattering is not prominent, and by a possible relative enrichment in CO_2 ice with respect to other units.

The major bright features seen on Titan generally do not have the same characteristics of Xanadu. As an example, from our analysis the southern Tsegihi feature, the second largest bright feature on Titan (also very bright at 5 μm), shows a low σ_0 backscattering coefficient ($\leqslant$0.10 on an average), that may be the result of a low regional roughness combined with a lower dielectric constant. It has a temperature some degrees lower than the antenna temperature measured in the nearby dark basins Fensal and Atzlan (the latter having an inlet that, right on the border of Tsegihi, shows an average antenna temperature as high as that of Shangri-La). On the other hand, the Dilmun feature, located at northern latitudes and centered in the anti-saturnian hemisphere, looks rather bright at 2.02, 2.69, 2.78 μm, while not having a significantly high backscattering coefficient (though higher than the coefficient measured on Tsegihi).

By considering a higher spatial resolution, the distinction between bright features and dark terrains is preserved; however, here surfaces with intermediate values of the variables considered

Table 6
Geophysical units explored in this work.

	I/F measured by VIMS				RADAR data	
	2.02 μm	2.69 μm	2.78 μm	~5 μm	σ_0	T_a (K)
Dark basins						
Shangri-La	0.06–0.08	0.02	0.02	0.02	0.13–0.15	95.4
Fensal	0.02	0.02	0.02	0.02	0.12	91.1
Atzlan (Tsegihi border)	0.08	0.02	0.02	0.03	0.04	95.4
Bright features						
Xanadu	0.12	0.03	0.03	0.04	0.61	87.8
Tsegihi	0.11	0.03	0.03	0.04	0.09	90.0
Adiri	0.13	0.02	0.03	0.03	0.30	87.8
Dilmun	0.13	0.03	0.03	0.04	0.19	92.2
Other units						
Huygens landing site	0.08	0.02	0.02	0.02	0.22	94.2
South-western border of Xanadu	0.11	0.03	0.03	0.04	0.11	87.8
Tortola Facula	0.07	0.02	0.02	0.02	0.19	91.8

also show up well. As an example, at a medium-to-high resolution scale, the Huygens landing site, located in between the Adiri eastern border and the Shangri-La dark basin, is in fact classified neither among the darkest terrains nor among the bright features; but it rather sits in a well populated group representing a transitional condition on the basis of all variables. In this spatial resolution range, we also find some homogeneous types made up of a few samples that are indicative of peculiar behaviors with respect to one or more variables: for example, correlations or anti-correlations between the reflectance observed at 2.02 μm and 5 μm, maybe due to a difference in composition. In the highest resolution data presented here, some of these types overlap with some *faculae*, showing different backscattering coefficients with respect to the surrounding terrains, but, at least in the case of Tortola Facula, with no clear evidence supporting very recent or ongoing cryovolcanic activity. Table 6 shows a summary of the main features analysed in this work.

Correlations between near-infrared and microwave properties of Titan's surface have been quantified here for the first time on the basis of medium resolution RADAR data and by means of an automatic classification method. The goal was to derive a general classification of the surface of Titan based on the clustering of measurement values in a multidimensional parameter space. Such correlations lead to the identification of regional geophysical units which are useful in constraining geophysical models describing the evolution of Titan's surface, but also to test the post-processing of RADAR data. The use of only five scatterometric passes for this work inevitably limits these results from the point of view of spatial coverage. However, our approach to the correlation of the data and subsequent multivariate classification can be expanded and refined as new data from the two instruments are released, adding new insights to the overall exploration of Titan that continues with the Cassini mission.

References

Acton, C.H., 1996. Ancillary data services of NASA's navigation and ancillary information facility. Planet. Space Sci. 44 (1), 65–70. doi:10.1016/0032-0633(95)00107-7.

Barnes, J.W., and 34 colleagues, 2005. A 5-micron-bright spot on Titan: Evidence for surface diversity. Science 310, 92–95. doi:10.1126/science.1117075.

Barnes, J.W., Brown, R.H., Soderblom, L., Buratti, B.J., Sotin, C., Rodriguez, S., Le Mouélic, S., Baines, K.H., Clark, R., Nicholson, P., 2007a. Global-scale surface spectral variations on Titan seen from Cassini/VIMS. Icarus 186, 242–258.

Barnes, J.W., 18 colleagues, and the Cassini RADAR Team, 2007b. Nearinfrared spectral mapping of Titan's mountains and channels. J. Geophys. Res. 112, E11006. doi:10.1029/2007JE002932.

Barnes, J.W., and 14 colleagues, 2009. Shoreline features of Titan's Ontario Lacus from Cassini/VIMS observations. Icarus 201, 217–225.

Barucci, M.A., Capria, M.T., Coradini, A., Fulchignoni, M., 1987. Classification of asteroids using G-mode analysis. Icarus 72, 304–324. doi:10.1016/0019-1035(87)90177-1.

Bianchi, R., Coradini, A., Butler, J.C., Gavrishin, A.I., 1980. A classification of lunar rock and glass samples using the G-mode central method. Moon Planets 22, 305–322. doi:10.1007/BF01259287.

Brown, R.H., and 21 colleagues, 2004. The Cassini Visual and Infrared Mapping Spectrometer (VIMS) investigation. Space Sci. Rev. 115 (1–4), 111–168. doi:10.1007/s11214-004-1453-x.

Carusi, A., Massaro, E., 1978. Statistics and mapping of asteroid concentrations in the proper elements space. Astron. Astrophys. Suppl. 34, 81–90.

Cerroni, P., Coradini, A., 1995. Multivariate classification of multispectral images: An application to ISM martian spectra. Astron. Astrophys. Suppl. 109, 585–591.

Coradini, A., Fulchignoni, M., Gavrishin, A.I., 1976. Classification of lunar rocks and glasses by a new statistical technique. The Moon 16, 175–190.

Coradini, A., Fulchignoni, M., Fanucci, O., Gavrishin, A.I., 1977. A FORTRAN V program for a new classification technique: The G-mode central method. Comput. Geosci. 3, 85–105.

Coradini, A., Giovannelli, F., Polimene, M.L., 1983. A statistical X-ray QSOs classification. In: International Cosmic Ray Conference Papers, vol. 1. Tata Institute of Fundamental Research, Bombay, pp. 35–38 (A85-22801 09-93).

Coradini, A., Cerroni, P., Forni, O., Bibring, J.-P., Gavrishin, A.I., 1991. G-mode classification of martian infrared spectral data from ISM-Phobos 2. Lunar Planet. Sci. 22, 243 (abstracts).

Coradini, A., and 34 colleagues, 2008. Identification of spectral units on Phoebe. Icarus 193 (1), 233–251.

Coustenis, A., and 10 colleagues, 2006. Titan's 3-micron spectral region from ISO high-resolution spectroscopy. Icarus 180, 176–185.

Elachi, C., and 21 colleagues, 2004. RADAR, the Cassini Titan RADAR Mapper. Space Sci. Rev. 115 (1–4), 71–110. doi:10.1007/s11214-004-1438-9.

Elachi, C., and 34 colleagues, 2005. Cassini Radar views the surface of Titan. Science 308, 970–974. doi:10.1126/science.1109919.

Erard, S., Cerroni, P., Coradini, A., 1991. Automatic classification of spectral types in the equatorial regions of Mars. American Astronomical Society, 24th DPS Meeting. Bull. Am. Astron. Soc., vol. 24, 978. Abstract 24.14-P.

Fulchignoni, M., and 42 colleagues, 2005. In situ measurements of the physical characteristics of Titan's environment. Nature 438 (7069), 785–791. doi:10.1038/nature04314.

Fussner, S., McEwen, A., Perry, J., Turtle, E., Dawson, D., Porco, C., West, R., and the Cassini ISS Team, 2005. Dependence of surface contrast on emission angle in Cassini 938-nm images of Titan. Lunar Planet. Sci. 36, March 14–18, 2005, League City, Texas. Abstract 2278.

Gavrishin, A.I., Coradini, A., Fulchignoni, M., 1980. Trends in the chemical composition of lunar rocks and glasses. Geokhimiia 1980, 359–370 (in Russian).

Gavrishin, A.I., Coradini, A., Cerroni, P., 1992. Multivariate classification methods in planetary sciences. Earth Moon Planets 59, 141–152. doi:10.1007/BF00058728.

Giovannelli, F., Coradini, A., Polimene, M.L., Lasota, J.P., 1981. Classification of cosmic sources – A statistical approach. Astron. Astrophys. 95, 138–142.

Hansen, G.B., 1997. The infrared absorption spectrum of carbon dioxide ice from 1.8 to 333 μm. J. Geophys. Res. 102 (E9), 21569–21587. doi:10.1029/97JE01875.

Hapke, B., 1993. Theory of Reflectance and Emittance Spectroscopy. Cambridge Univ. Press, Cambridge, UK. ISBN-13: 9780521619271, ISBN-10: 0521619270.

Hapke, B., 2008. Bidirectional reflectance spectroscopy: 6. Effects of porosity. Icarus 195, 918–926.

Hayne, P., McCord, T.B., Barnes, J.W., 2009. Titan's near infrared atmospheric transmission and surface reflectance from the Cassini Visual and Infrared Mapping Spectrometer. Lunar Planet. Sci. 40 (Lunar Planet. Sci. XL), March 23–27, 2000, The Woodlands, Texas. Abstract 1863.

Heiles, C.E., Drake, F.D., 1963. The polarization and intensity of thermal radiation from a planetary surface. Icarus 2, 281–292.

Janssen, M.A., Paganelli, F., Lorenz, R.D., and the Cassini RADAR Science Team, 2006. Dielectric properties of Titan's surface using the Cassini RADAR radiometer. American Astronomical Society, 38th DPS Meeting. Bull. Am. Astron. Soc. 38, 586. Abstract 56.06.

Janssen, M.A., 17 colleagues, and the Cassini RADAR Team, 2009a. Titan's surface at 2.2-cm wavelength imaged by the Cassini RADAR radiometer: Calibration and first results. Icarus 200, 222–239.

Janssen, M.A., Le Gall, A., Wye, L.C., Zebker, H.A., Lorenz, R.D., Paillou, P., Paganelli, F., and the Cassini RADAR Team, 2009b. Anomalous radar backscatter from Titan's Xanadu. Lunar Planet. Sci. 40, Houston, TX.

Jennings, D.E., and 19 colleagues, 2009. Titan's surface brightness temperatures. Astrophys. J. 691, L103–L105. doi:10.1088/0004-637X/691/2/L103.

Le Gall, A., Janssen, M.A., Lorenz, R.D., Zebker, H., Wye, L., Paillou, P., 2009. Radar-bright channels on Titan. Lunar Planet. Sci. 40, Houston, TX.

Le Mouélic, S., and 17 colleagues, 2008. Joint analysis of Cassini VIMS and RADAR data: Application to the mapping of Sinlap crater on Titan. J. Geophys. Res. 113, E04003. doi:10.1029/2007JE002965.

Lopes, R.M.C., and 43 colleagues, 2007. Cryovolcanic features on Titan's surface as revealed by the Cassini Titan Radar Mapper. Icarus 186, 395–412.

Lorenz, R.D., 11 colleagues, and the Cassini RADAR Team, 2007. Titan's young surface: Initial impact crater survey by Cassini RADAR and model comparison. Geophys. Res. Lett. 34, L07204. doi:10.1029/2006GL028971.

McCord, T.B., and 24 colleagues, 2004. Cassini VIMS observations of the Galilean satellites including the VIMS calibration procedure. Icarus 172, 104–126.

McCord, T.B., 16 colleagues, and the Cassini VIMS Team, 2006. Composition of Titan's surface from Cassini VIMS. Planet. Space Sci. 54, 1524–1539. doi:10.1016/j.pss.2006.06.007.

McCord, T.B., 12 colleagues, and the Cassini VIMS Team, 2007. Titan's surface: Search for spectral diversity and composition using the Cassini VIMS investigation. Icarus 194, 212–242.

Miller, E., and 18 colleagues, 1996. The Visual and Infrared Mapping Spectrometer for Cassini. Proc. SPIE 2803, 206–220.

Negrão, A., 2007. The Characterisation of Titan's Lower Atmosphere and Surface from Near-Infrared Spectra. Ph.D. thesis, Universidade de Lisboa, Faculdade de Ciências, Departamento de Física.

Niemann, H.B., and 17 colleagues, 2005. The abundances of constituents of Titan's atmosphere from the GCMS instrument on the Huygens probe. Nature 438, 779–784. doi:10.1038/nature04122.

Orosei, R., Bianchi, R., Coradini, A., Espinasse, S., Federico, C., Ferriccioni, A., Gavrishin, A.I., 2003. Self-affine behavior of martian topography at kilometer scale from Mars Orbiter Laser Altimeter data. J. Geophys. Res. 108 (E4). doi:10.1029/2002JE001883.

Perry, J.E., McEwen, A.S., Fussner, S., Turtle E.P., West, R.A., Porco, C.C., Knowles, B., Dawson, D.D., and the Cassini ISS Team, 2005. Processing ISS images of Titan's surface. Lunar Planet. Sci. 36, March 14–18, 2005, League City, Texas. Abstract 2312.

Porco, C.C., and 35 colleagues, 2005. Imaging of Titan from the Cassini spacecraft. Nature 434 (7030), 159–168. doi:10.1038/nature03436.

Rodriguez, S., Le Mouélic, S., Sotin, C., Clénet, H., Clark, R.N., Buratti, B.J., Brown, R.H., McCord, T.B., Nicholson, P.D., Baines, K.H., and the VIMS Science Team, 2006. Cassini/VIMS hyperspectral observations of the Huygens landing site on Titan. Planet. Space Sci. 54 (15), 1510–1523. doi:10.1016/j.pss.2006.06.016.

Soderblom, L.A., Brown, R.H., and the Cassini VIMS Investigation Team, 2005. Deconvolution of Cassini VIMS Titan cubes into atmospheric spectral scattering, surface topographic, and surface spectroscopic components. Lunar Planet. Sci. 36, March 14–18, 2005, Houston, TX. Abstract 1869.

Soderblom, L.A., and 26 colleagues, 2007. Correlations between Cassini VIMS spectra and RADAR SAR images: Implications for Titan's surface composition and the character of the Huygens probe landing site. Planet. Space Sci. 55, 2025–2036. doi:10.1016/j.pss.2007.04.014.

Sotin, C., and 25 colleagues, 2005. Release of volatiles from a possible cryovolcano from near-infrared imaging of Titan. Nature 435, 786–789. doi:10.1038/nature03596.

Stiles, B., 13 colleagues, and the Cassini RADAR Team, 2008. Determining Titan's spin state from Cassini RADAR images. Astron. J. 135, 1669–1680. doi:10.1088/0004-6256/135/5/1669.

Thekaekara, M.P., 1973. In: Drummond, A.J., Thekaekara, M.P. (Eds.), The Extraterrestrial Solar Spectrum. Institute of Environmental Sciences, Mount Prospect, Illinois. p. 114.

Tomasko, M.G., and 39 colleagues, 2005. Rain, winds and haze during the Huygens probe's descent to Titan's surface. Nature 438, 765–778. doi:10.1038/nature04126.

Tosi, F., Coradini, A., Gavrishin, A.I., Adriani, A., Capaccioni, F., Cerroni, P., Filacchione, G., Brown, R.H., 2005. G-mode classification of spectroscopic data. Earth Moon Planets 96, 165–197. doi:10.1007/s11038-005-9061-7.

Tosi, F., Turrini, D., Coradini, A., Filacchione, G., 2010. Probing the origin of the dark material on Iapetus. MNRAS, in press. doi:10.1111/j.1365-2966.2010.16044.x.

Turtle, E.P., Perry, J.E., McEwen, A.S., DelGenio, A.D., Barbara, J., West, R.A., Dawson, D.D., Porco, C.C., 2009. Cassini imaging of Titan's high-latitude lakes, clouds, and south-polar surface changes. Geophys. Res. Lett. 36, L02204. doi:10.1029/2008GL036186.

Ulaby, F.T., Moore, R.K., Fung, A.K., 1981. Microwave Remote Sensing. Active and Passive, vol. I. Addison-Wesley Publ. Company, Reading, MA.

Ulaby, F.T., Moore, R.K., Fung, A.K., 1982. Microwave Remote Sensing. Active and Passive, vol. II. Addison-Wesley Publ. Company, Reading, MA.

Website of the ISIS software: <http://isis.astrogeology.usgs.gov>.

Website of the NASA's Planetary Data System database: <http://pds.jpl.nasa.gov>.

West, R., and 19 colleagues, 2009. Cassini RADAR sequence planning and instrument performance. IEEE Trans. Geosci. Remote Sens. 47 (6), 1777–1795. doi:10.1109/TGRS.2008.2007217.

White, T.L., Cogdell, J.R., 1973. Lunar polarization studies at 3.1 mm wavelength. The Moon 6, 235–249. doi:10.1007/BF00562205.

Wood, C.A., Lorenz, R., Kirk, R., Lopes, R., Mitchell, K., Stofan, E., and the Cassini RADAR Team, 2009. Impact craters on Titan. Icarus, in press.

Wye, L.C., Zebker, H.A., Ostro, S.J., West, R.D., Gim, Y., Lorenz, R.D., and the Cassini RADAR Team, 2007. Electrical properties of Titan's surface from Cassini RADAR scatterometer measurements. Icarus 188, 367–385.

Wye, L., Zebker, H.A., Lopes, R.M., Peckyno, R., Le Gall, A., Janssen, M.A., 2008. A backscatter analysis of Titan's surface features & their global distribution using Cassini RADAR data. American Astronomical Society, 40th DPS Meeting. Abstract 31.22.

Zebker, H.A., Wye, L.C., Janssen, M.A., and the Cassini RADAR Team, 2008. Titan's surface from reconciled Cassini microwave reflectivity and emissivity observations. Icarus 194, 704–710.

Zebker, H., Stiles, B., Hensley, S., Lorenz, R., Kirk, R.L., Lunine, J.I., 2009. Size and shape of Saturn's moon Titan. Science 324, 921–923. doi:10.1126/science.1168905.